MASTER'S THESIS IN APPLIED MECHANICS

Implementation of Dynamic Contact Angle for Multiphase Simulation of Rain Film Contamination on 5G-Radomes

LOVE ERIKSSON
PATRICIA VANKY

Department of Mechanics and Maritime Sciences
Division of Fluid Dynamics
CHALMERS UNIVERSITY OF TECHNOLOGY

Göteborg, Sweden 2020

Implementation of Dynamic Contact Angle for Multiphase Simulation of Rain Film Contamination on 5G-Radomes
LOVE ERIKSSON
PATRICIA VANKY

Master's thesis 2020:28
Department of Mechanics and Maritime Sciences
Division of Fluid Dynamics
Chalmers University of Technology
SE-412 96 Göteborg
Sweden
Telephone: +46 (0)31-772 1000

Chalmers Reproservice
Göteborg, Sweden 2020

Implementation of Dynamic Contact Angle for Multiphase Simulation of Rain Film Contamination on 5G-Radomes
Master's thesis in Applied Mechanics
LOVE ERIKSSON
PATRICIA VANKY
Department of Mechanics and Maritime Sciences
Division of Fluid Dynamics
Chalmers University of Technology

Abstract

The aim of this thesis is to simulate the behaviour of water films created by precipitation on 5G-radomes. This is done to predict the reduction of transmission and receiving range as a product of the water absorbing the high frequency microwaves.

To describe the proper behaviour of rain droplet spread and water films, impingement onto a variation of surfaces is simulated in the commercial software ANSYS Fluent and validated against experimental data. Simulations are conducted using a direct numerical simulation method for multiphase flow, Volume of Fluid, VoF, and the surface tension is modelled using the continuum surface force method. The contact angle is implemented as boundary conditions for the continuum surface force method at the contact line between the two phases and the wall. For this thesis, a dynamic contact angle model is implemented as a user defined function. Whether the liquid spread is advancing or receding is then determined by the contact line velocity direction as well as the volume fraction gradient direction. Implemented dynamic contact angle models are validated with separate convergence studies for simulation of water droplet impingement onto a variation of hydrophobic surfaces in addition to the validation against experimental data. Additionally, the effects of implementing a Navier-slip boundary condition, relaxing the no-slip boundary was evaluated. Furthermore, the dynamic contact angle model is tried for simulation of water films.

The implementation of the dynamic contact angle gives simulated results that closely match the behaviour shown in experiments of droplet impingement for most cases tested. However, the simulations of high Weber number impacts onto a hydrophobic surface result in a splashing effect not seen in experiments. Also, the hydrophilic surfaces used in the experiments have such low contact angles that resolving the curvatures gives instabilities. The results for hydrophilic surfaces are therefore not optimal to consider. It was also found that the results are dependent on the mesh, especially the boundary layer treatment. Using a polyhedral mesh with 5 prism layers resulted in good results whereas other refinement approaches need more work.

Water film simulations were conducted as a proof-of-concept to test the implemented dynamic contact angle models on complex domains with sharp transitions and variations of hydrophobicity. It was shown that the models can handle water over these complex areas and they are therefore ready to be used when methods for properly injecting full scale rain onto the surface are developed.

Keywords: Wettability, Dynamic Contact Angle, Droplet Impingement, Surface Tension, ANSYS Fluent, Computational Fluid Dynamics, CFD, Multiphase Flow, Volume of Fluid, VoF

Preface

The idea for this thesis sprung from a desire at Ericsson AB to be able to simulate rain. This as the water film caused by rain negatively impacts the microwave transmission with a varied effect on the range depending on what form the water film takes.

Simulating rain consists of a multitude of steps, from generating the actual raindrops and the density of the rain to handling the behaviour of the water running along the surface it is subjected to and the phenomena happening in between. Due to the magnitude of the problem statement, the project was limited to simulating the droplet impinging onto a variation of surfaces.

As it so often does, even the limited scope turned out to be much larger and more complex than imagined. During the project several unexpected and interesting problems occurred, that unfortunately fell outside of the scope of the project but would have been interesting to investigate further. With this thesis we can, however, present a first step where the results have been verified for single droplets of water, and the models have been tested for larger films without being able to properly validate what was found.

Acknowledgements

We would like to acknowledge the aid of our supervisors at Ericsson AB, Peter Melin, Erik Karlsson and Fredrik Öhrby, for their invaluable assistance in the project. We also want to show our deepest gratitude to ANSYS, specifically Anna Kvarnström for her continuous encouragement and support, as well as Adam Anderson for his help in developing the User Defined Function used in the project. Lastly, we want to thank our examiner, Srdjan Sasic, for his assistance and advice.

Contents

1 Introduction

This chapter gives an introductory background and the reasoning behind the research and simulations done during this project. The limitations and a brief description of the methodology of the project is also described.

1.1 Background

As a connected society, with smartphones, smart homes and robots on factory floors are becoming a larger part of our everyday lives, the need for 5G coverage is greatly increasing. According to a report published by Ericsson AB (Cerwall et al., 2019), the 5G-network has the potential to reach 65% of the worlds population and stand for nearly half of the mobile data traffic world wide in the year 2025. The need for full coverage over large areas, such as long stretches of highway and over airports, becomes critical with the implementation of autonomous vehicles, where the 5G-network is a crucial part.

This wide deployment of 5G generates new obstacles for the telecommunication industry to face and overcome. The 5G network uses higher frequencies than previous generations, resulting in a shorter range of reach. When the 5G-radomes and antennas are subjected to precipitation, the reaching range is decreased even further (Grémont & Filip, 2004). This is due to a phenomenon called rain fade, meaning that the transmitting and receiving microwaves are absorbed by the water in the atmosphere and the water film that the rain produces on the surface of the radomes. Knowledge about how to set up better simulations of rain films on antennas and radomes is therefore needed to properly determine the actual range of reach when subjected to weather.

The behaviour of the water film on the radome surface dictates how the range is affected. The thickness of the water film is one of several factors that is of interest (Moroder, Siart, Chwala, & Kunstmann, 2017). The thicker the water film gets, the more the range will be affected. However, water formation on the surface of a radome can take several forms, such as droplets, rivulets, and full or partial films. For a partially wet surface the range is less affected than for a fully wet surface, even if the amount of water on the radome is the same (Salazar-Cerreño et al., 2014). Which of these forms the rain takes when in contact with a surface is largely determined by the properties of the surface. The main property being the hydrophobicity, which determines how water-repellent the surface is. In general, full and partial water films with permanent rivulets are formed when a non-water repellent surface is subjected to heavy rain falls (Fenn, 1997), whereas a higher hydrophobicity and lighter rain is more likely to yield dispersed droplets on the surface.

1.2 Purpose

The aim of the thesis is to research models that would accurately simulate the physics of water in contact with a surface. This includes the physical phenomena upon impact between water droplet and surface as well as the spreading behaviour upon impact. A theoretical study of models used to simulate these phenomena will be conducted. Additionally, the models are to be implemented into the commercial software ANSYS Fluent and validated against experimental data. The purpose of this thesis is not to develop a full scale simulation of rain, but rather to build an understanding about what surface properties affect the rain droplet behaviour upon impingement onto a surface and what form the water film takes on that surface.

1.3 Methods

In this thesis, dynamic contact angle models has been evaluated as a means to describe surface properties. Appropriate models were chosen and implemented as a User Defined Function in ANSYS Fluent. The implemented dynamic contact angle model was compared to corresponding static contact angles and further validated against experimental data for a variation of surfaces. Furthermore, effects of relaxing the no-slip boundary on the impingement surface was evaluated. Finally the models were used for a water film case on a part of a radome, as a means to evaluate the behaviour for larger amount of water over a complex domain.

1.4 Limitations

As stated above the simulations done in the thesis work are limited to the use of ANSYS Fluent and the functionality offered in the software. Potential implementation of models will only consider established models available in literature, as no new models will be developed. As wetting of dry surfaces due to precipitation is caused by the impingement of individual droplets and the subsequent spread of the droplets due to surface properties, the simulations will only be conducted on individual droplets impacting dry surfaces.

As experiments on water film behaviour on a surface has only been found for very large scales, with domains of several meters. Validation of implemented models on water films fall outside of the scope for this thesis as well. Such simulations will be performed on smaller domains as a proof-of-concept.

2 Theory

Evaluation of how precipitation builds up water films on a surface requires knowledge about the rain, droplet physics and properties of said surface. This chapter gives a theoretical introduction into these areas and how they affect the final water film.

2.1 Rain

Water film build up on surfaces due to precipitation is heavily dependent on the size and space distribution of the impinging rain droplets. The spacing is necessary to determine the number of droplet injection points needed, and the droplet sizing is used to achieve a correct volume of water for each impinging droplet. These distributions may be divided into several regimes. Rain that would be perceived as heavy usually has a droplet diameter of between four and five millimetres, whereas for a light drizzle, the droplets would be about half a millimeter in diameter. The spread between drops is seldom less than 17.5 times the diameter of the drop (Bilanin, 1987), meaning that the perception of the rain is mostly based on droplet sizing. Since the spacing of droplets is rather large in an usual rain environment, the mixture of air and water may be considered dilute, and the collisions between droplets may be neglected for simplicity (Wu, 2018). Measurements of rain is commonly performed using a rain gauge, which describes the rain in terms of a length measurement. Moderate rain is usually defined to be between 2.5 and 7.6 mm/h (Jebson, 2007).

The velocity of the impinging rain droplets is between $2 - 9$ m/s, and can be directly associated with the size of the drop (Serio, Carollo, & Ferro, 2019). For small droplets, the initial speed can be assumed to be of the same order as the local air velocity, and thus generally the trajectory of the local air velocity. The inertia of larger droplets is strong enough for the droplets to deviate from the local air velocity, and may be defined using graviational forces, buoyancy and drag. For droplets in free fall that exceed 9 m/s, the droplet will break into several smaller droplets and the velocity is decreased.

In droplet physics, the inertial forces can be related to the surface tension of the drop by a non-dimensional number called Weber number, further explained in section 2.2.2. This relation can then give an indication on how a drop will splash upon impact with a surface. A higher Weber-number means that the inertia is more dominant which will result in the splashing effect being larger. For rain in general, the Weber number has a large range from about 50 for light rain to 12000 for heavier rain (Nouhou Bako, Darboux, James, Josserand, & Lucas, 2016).

Simulations of droplet impingement on surfaces is a highly dynamic event, dominated by an intricate relationship between inertial, viscous and surface tension forces. To be able to capture all the relevant droplet physics of the impingement event the temporal- and spatial resolution is under high demand. Therefore it is desired for the simulations to be conducted on a per-particle basis.

2.2 Droplet Physics

Fluid dynamics is the field of physics concerned with mechanics of fluids. Multiphase flow is a certain branch of fluid dynamics which is characterized by the coexistence of several different phases in a domain. Liquid, gas and solid phases may all have an influence on the flow field, in comparison to single-phase flows, which only contain a single fluid phase (Yadigaroglu & Hewitt, 2017). In general, the phases are represented by a volume fraction, α, which is the space fraction occupied by that specific phase. Interfaces are of vital importance in multiphase flow, and are defined as the boundaries between the different phases. Importantly, the interfaces are not known a priori, and are as such a part of the solution. As simulations of water film build up on surfaces are characterized by multiple phases coexisting in a domain, this is commonly modelled as a multiphase flow where the impinging droplets are treated as one phase and the local air as a second phase.

2.2.1 Surface Tension

The shape of the interface between two fluids is determined by a balance of inertial, viscous and surface tension forces acting upon it. For any liquid, the surface tension can be described as the work which must be supplied in order to increase the surface area by one unit (de Gennes, Brochard-Wyart, & Quere, 2003). Microscopically, the droplet can be seen as an aggregate of molecules which are attracted to each other. At the interface there are exposed liquid molecules that have less neighbouring liquid molecules creating an imbalance, as can be seen in Figure 2.1. This imbalance causes the liquid molecule to pull inwards towards the center of the liquid. If the droplet maintains a spherical shape, there is a net balance of cohesive forces. Effectively, this means that droplets adjust their shape in order to decrease their surface area.

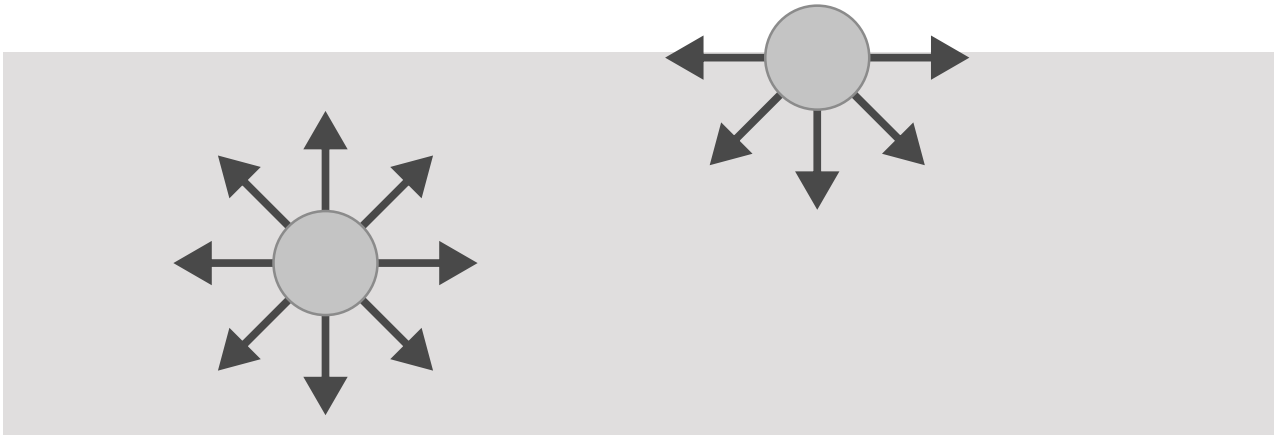

Figure 2.1: *Intermolecular forces acting at the liquid molecules at an interface between liquid and gas.*

The surface tension of water is at room temperature is 0.0728 N/m, which is relatively high in comparison to most other liquids. This is due to the water molecules having a high attraction to each other because of the hydrogen bonds.

2.2.2 Non-dimensional Numbers

Droplet behaviour may be characterized using a variation of non-dimensional numbers, as fluid behaviour may differ heavily depending on the scale of these non-dimensional number (Rapp, 2016). Moreover, the non-dimensional numbers are constructed in order to exploit similarity, which means that two systems with different length scales are mechanically similar if their non-dimensional numbers are equal. Generally, the particle Reynolds number is used to describe the effects of viscous to inertial forces, and as a measurement of the turbulence in a flow.

$$Re = \frac{Inertial\ forces}{Viscous\ forces} = \frac{\rho_l U L}{\mu_l} \tag{2.1}$$

where ρ and μ are the density and kinematic viscosity of the continuous phase, respectively. U is the relative velocity between the continuous phase and the particle, in this case the droplet, and the characteristic length scale L is defined depending on the flow situation to relate the geometry of the flow to the viscous and inertial forces. For particulate flow the characteristic length is the diameter of the particle.

A non-dimensional number which is of particular importance in droplet physics is the Weber number, which relates the inertial forces to the surface tension (Rapp, 2016).

$$We = \frac{Inertial\ forces}{Surface\ tension} = \frac{\rho_l U^2 L}{\sigma_{lg}} \tag{2.2}$$

where ρ_l, is the density of the droplet fluid, U the droplet velocity and σ the liquid-gas surface tension. The Weber number will describe the droplets ability maintain its spherical shape and to stay intact meaning that it can give insight into whether the droplet will splash or not upon impact with a wall.

A further non-dimensional number of importance is the Ohnesorge number, which relates Reynolds and Weber number. Physically it relates the viscous forces to the product of the surface tension and inertial forces (Rapp, 2016).

$$Oh = \frac{Viscous\ forces}{Surface\ tension \cdot Inertial\ forces} = \frac{\mu_l}{\sqrt{\rho_l \sigma_{lg} L}} = \frac{\sqrt{We}}{Re} \tag{2.3}$$

The Ohnesorge number can be used to determine what regime a droplet is interacting in (Schiaffino & Sonin, 1997). A larger Oh-number will indicate a greater influence of the viscosity.

Finally, the capillary number is also of great importance in situations with significant surface tension, as it relates the viscous forces to surface tension (Rapp, 2016).

$$Ca = \frac{Viscous\ forces}{Surface\ tension} = \frac{\mu_l U}{\sigma_{lg}} \tag{2.4}$$

A low capillary number indicates that the flow is dominated by capillary forces, whereas a high capillary number indicates that the capillary forces are negligible in comparison to viscous forces.

2.2.3 Surface Wetting

Wetting occurs when a droplet impinges on a solid surface and subsequently spreads out over the surface (de Gennes et al., 2003). In essence, wetting is a phenomenon defined by contact between three phases: Liquid, gas, and solid. Depending on the properties of the surface, the liquid phase may spread out in different amounts. It may be totally wetting, forming a microscopic film over the surface, or it may be partially wetting, which is characterised by a much larger fluid thickness. For partially wetting flows, the triple-line of contact between the surface, liquid and gas phases is called the contact line and can be seen in Figure 2.2.

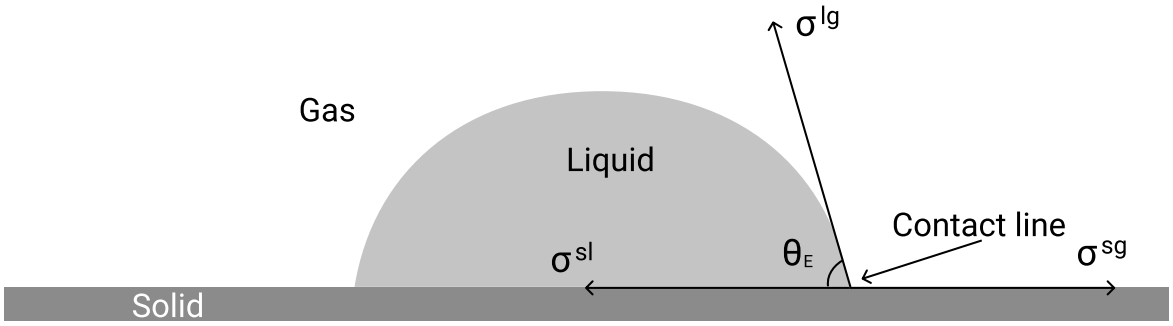

Figure 2.2: *Contact line between three phases and corresponding equilibrium contact angle. θ_E refers to the contact angle and σ_{lg}, σ_{sl} and σ_{sg} the surface tensions between the liquid-gas, liquid-solid and solid-gas phases respectively.*

2.2.3.1 Contact Line and Contact Angle

For all wetting phenomena in rest there exists a specific equilibrium contact angle, which is the angle between the surface and the liquid-gas surface tension force. It can be defined using Young's Equation which relates the equilibrium contact angle to the surface tension forces of the three different phases (Young, 1805; Göhl, Mark, Sasic, & Edelvik, 2018).

$$\sigma_{lg} \cos(\theta_E) = \sigma_{sg} - \sigma_{sl} \tag{2.5}$$

where σ_{lg}, σ_{sl} and σ_{sg} are the surface tensions between the liquid-gas, liquid-solid and solid-gas phases respectively.

The angle between the surface and contact line, may vary depending on if the droplet and its corresponding contact line is in rest. These contact angles are referred to as static and dynamic. As can be seen in Figure 2.3, it is assumed that the contact angle at the smallest, microscopic scale is equal to the equilibrium contact angle θ_E (Afkhami, Zaleski, & Bussmann, 2009). At larger scales, the contact angle may differ due to surface roughness of heterogeneities, which results in the need to model the dynamic contact angle θ_D. The apparent contact angle θ_{app}, which is determined at macro scale, is used to interpret experimental or numerical results and is measured at a finite distance from the interface.

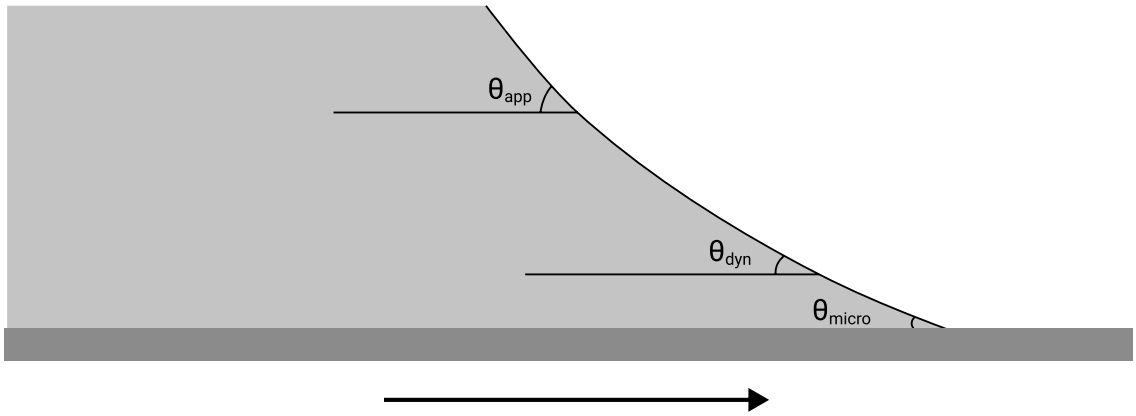

Figure 2.3: *Contact angles at different scales for liquid on a moving wall.*

When a droplet moves on a surface, the droplet must both advance and recede which means that the contact angle may also be divided into receding or advancing, as shown in Figure 2.4. The advancing contact angle is defined as the largest static contact angle before the contact line starts wetting the surface. Furthermore, the receding contact angle is defined as the smallest contact angle as the contact line recedes over the surface (Göhl et al., 2018).

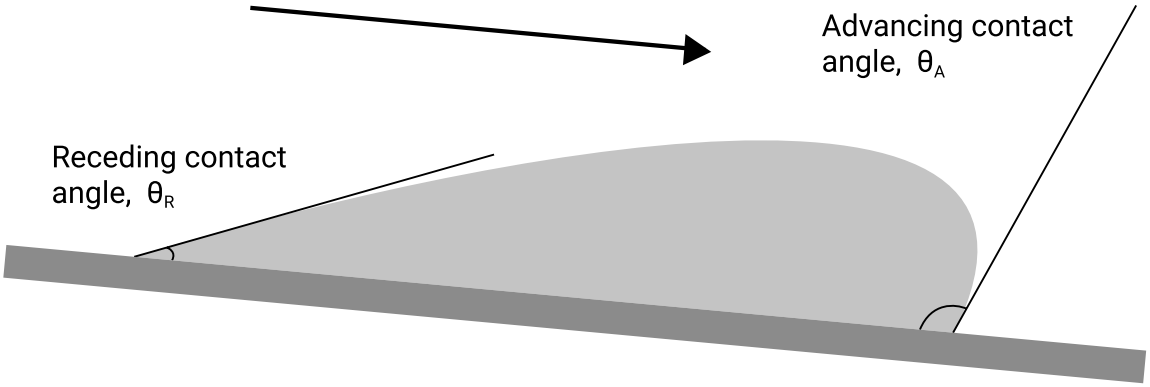

Figure 2.4: *Advancing and receding contact angles of droplet in motion over a plate.*

The difference between advancing and receding contact angles is called contact angle hysteresis and is central for movement of a droplet. For a droplet in rest upon a surface, it is possible to describe its shape with the equilibrium contact angle which is constant along the contact line. However, as soon as it breaks equilibrium, the contact angles and contact line become dynamic and the contact angle hysteresis is present. In order to properly predict the motion of the droplets upon the surface, accurate solution of the dynamic contact angle and the velocity of the contact line is necessary.

2.2.3.2 Surface Properties

The properties of the surface have large influences on the dynamics of the droplet. For example, the hydrophobicity of the surface will influence the wettability of single droplets the surface as can be seen in Figure 2.5. The hydrophobicity may be defined using the equilibrium contact angle, where low contact angles, $\theta_E < 90°$, yield a hydrophilic surface with high wettability and a high contact angle, $\theta_E > 90°$, yields a hydrophobic surface with low wettability (de Gennes et al., 2003). This will fundamentally change how the droplets move upon the surface.

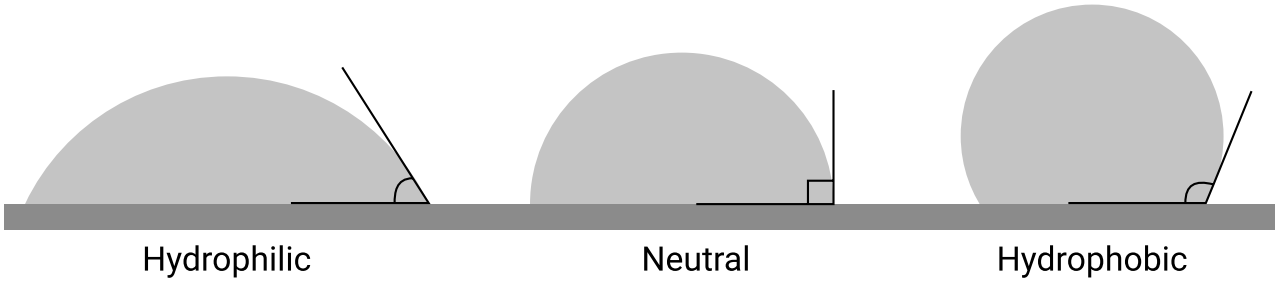

Figure 2.5: *Hydrophobicity of a droplet.*

Additionally, the hydrophobicity of the surface will determine the water formation on the surface for larger amounts of water. A hydrophilic surface is more likely to form a film than a hydrophobic surface that repels the water yielding a partially wet surface (Fenn, 1997). Surfaces with a very high contact angles, $\theta_E > 135°$, sometimes referred to as superhydrophobic, are commonly used on exteriors of radomes as they minimize the formation of a continuous water film (Salazar-Cerreño et al., 2014).

2.2.3.3 Surface Weathering

As mentioned, hydrophobic and superhydrophobic surfaces are often used to prevent water film formation. However, studies show that the hydrophobic permanence can be questioned, as it has been shown to degrade over time as the surface is subjected to temperature, humidity, ultraviolet rays, air pollution, and dust (Salazar-Cerreño et al., 2014). It has been shown, that the contact angle of hydrophobic radomes can reduce as much as 30° in less than 9 months when subjected to weather and pollution (Weigand, 1973).

2.2.4 Droplet Impact and Spread

The impact of droplets upon a dry surface have a wide range of documented phenomenon. Depending on the impacting energy, the droplet may deposit onto the surface, it may bounce and partially rebound, and may form a Worthington jet in its center. It may contact and spread out in finger-like lamellar structures, or it may splash and disintegrate into several smaller droplets (Rein, 1993). These described phenomena are illustrated and can be seen in Figure 2.6.

There are three forces involved in the droplet spreading, the hydrodynamic pressure, $f_p = \rho U^2 D^2$, the surface tension force, $f_\sigma = \sigma D$, and the viscous force, $f_{vis} = \eta U D$ (Zhou, Loney, Fedorov, Degertekin, & Rosen, 2012). As the droplet spreads, it is forced to deviate from its equilibrium shape by the hydrodynamic force while the surface tension force aims to restore the equilibrium shape. Meaning that when the hydrodynamic force is larger than the surface tension, the drop will deform, the kinetic energy dissipated by the viscous force and transferred to surface energy so that the hydrodynamic force is decreased and the surface tension force increased. When the hydrodynamic force reduces below the surface tension force, the droplet starts to relax back to its equilibrium shape. The surface energy will be transferred back to kinetic energy, the hydrodynamic force will then increase again and if it becomes larger than the surface tension force, the process will be repeated until all kinetic energy is dissipated. This means that in the inertial regime where the viscous effects are negligible, the drop will oscillate around its equilibrium shape.

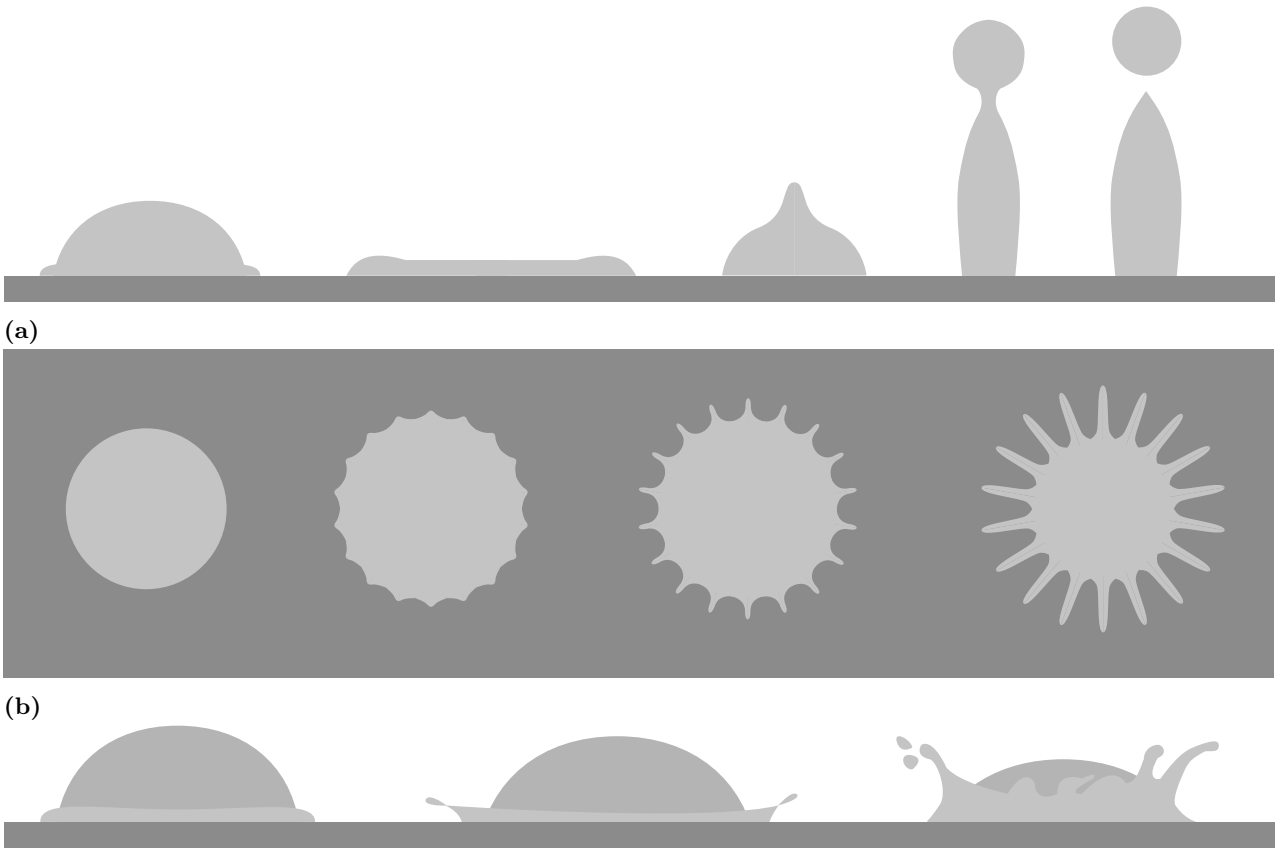

Figure 2.6: *Three droplet impingement phenomena, (a) side view of impingement with partial rebound and worthington jet, (b) top view of impingement with lamellar spread and (c) side view of impingement with splash.*

These spreading dynamics at impact are mainly characterized by the Weber and Ohnesorge numbers (Schiaffino & Sonin, 1997). From experiments by Ersoy and Eslamian (2020), it can be seen that the impact grows more energetic with increasing Weber number as it scales the hydrodynamic forces spreading the drop. Meaning that for high Weber numbers, the spread is driven radially outwards by large hydrodynamic forces induced by the impact. At these high impact energies, splashing phenomenon is prevalent, and the remainder of the droplet after splash may form a completely wetting film (Moreira, Moita, & Panao, 2010). For droplets impinging at moderate impact velocities, the spread is still dominated by hydrodynamic forces but capillary instabilities may deform the rim of the impacting droplet and give rise to lamellar structures, as seen in Figure 2.6b. As these lamellar structures stretch, smaller droplets may pinch off due to interfacial instabilities (Ersoy & Eslamian, 2020). For droplets impacting at lower Weber numbers, the spread is instead driven by the capillary forces pulling the liquid, and is therefore less affected by impact velocity. For these lower impact velocities, the droplet may partially rebound off the surface. This may occur when the droplet impacts a dry surface and a gas interlayer forms between the surface and the impacting droplet (Šikalo, Tropea, & Ganić, 2005). During partial rebound with a solid surface, the droplet may give rise to a Worthington jet, as can be seen in Figure 2.6a. However, the exact mechanics behind the jet occuring upon impingement are mostly unknown. What has been shown, is that the jet occurs only for a limitied range of low Weber number impacts in the order of $10^0 - 10^1$ (Yamamoto, Motosuke, & Ogata, 2018). If the impact energy is high enough during the partial rebound, one or multiple drops may be detached from the top of the jet. This phenomenon is highly dependent on capillary instabilites. If the present gas interlayer between the impacting droplet and the surface is punctured, complete deposition of the droplet upon the surface may occur.

In contrast to the Weber number, the Ohnesorge number scales the spread-resisting force. At high Ohnesorge numbers, the resistance is viscosity, while for low Ohnesorge numbers, the resistance is inertia. From the

relation between these parameters, Schiaffino and Sonin (1997) has divided the spread into four regimes, as can be seen in Figure 2.7. The four regimes are described below.

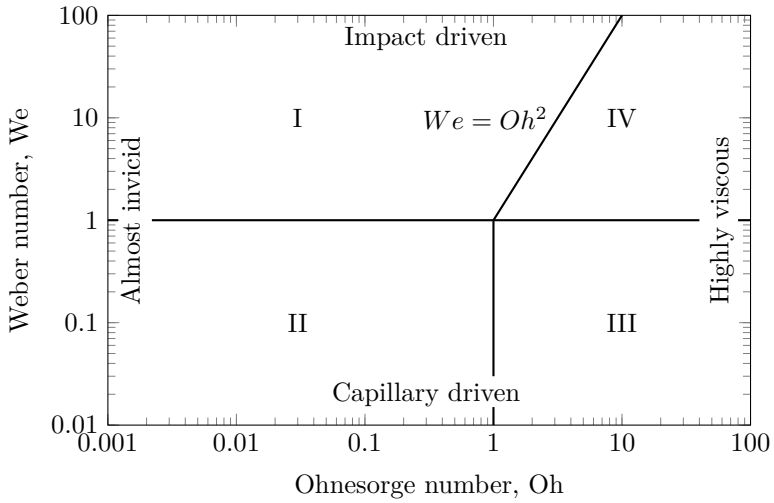

Figure 2.7: *Regime map for droplet spreading. Redrawn from Schiaffino and Sonin (1997)*

Region I can be defined as inviscid and impact-driven. The spreading mainly occurs over a short time period in which the flow is driven by the dynamic pressure of impact and inertia is the main resisting force. Initially, the viscous forces are negligible and the drop size and impact velocity dictates the velocity of spread. Over time, after the main spreading is over, the viscous effects are no longer negligible and dampens the oscillations on a timescale much longer than the spreading time.

Region II is still inviscid but is instead driven by the capillary forces. The impact velocity is not deciding the spreading velocity in this region but most of the spreading is driven by the imbalance of capillary forces at the contact line, again resisted by inertia. As in region I, viscous force has a mild dampening effect on the oscillations.

Region III is highly viscous and capillarity-driven. Again, the spreading is driven by the imbalance of capillary forces at the contact line, but is instead resisted by the viscosity. Impact velocity is negligible and inertial oscillations are not present.

Region IV is driven by the impacting velocity but is highly viscous. The spreading is therefore driven by the dynamic pressure of impact, but the viscous shear is resisting the flow instead of inertia. The effect of capillary force on the spreading is negligible. As in region III there is no presence of oscillations.

In the later stages of droplet spreading, the hydrophobicity of the surface plays a key role in determining whether the droplet will recoil or spread out on the surface, as it determines when the contact line will stop moving as the droplet reaches an equilibrium state (Schiaffino & Sonin, 1997). This will determine the overall wetted surface when a droplet impinges upon a surface. As more and more droplets repeatedly impact a surface, the consecutive wetting of the dry surface may conjoin the individual wetted surfaces into a liquid film. This has a significant effect on the impact phenomena of the droplets (Ersoy & Eslamian, 2020). Depending on the thickness of this film, the effects of wall adhesion on the impacting droplets decrease. In general, the behaviour of droplet impingement onto already wetted surfaces may be divided into four different regimes (Moreira et al., 2010). For very thin films, the droplet behaviour depends largely on surface properties, i.e. roughness or hydrophobicity. As the thickness of the film is increased due to more droplets impinging on the surface, or droplets conjoining into thicker films, the influence of the surface properties is reduced. For a thick film, the behaviour no longer depends on the surface properties, and is instead a function of the film thickness. When the film becomes so thick that it can be described as a deep pool, the droplet behaviour is no longer dependent on either surface topography, or film thickness.

3 Numerical Modelling

This chapter describes the procedure for modelling the physics needed to conduct simulations of droplet impact and spread over a surface.

3.1 Governing Equations

Fluid dynamics are governed by a set of equations for conservation of momentum, energy and mass, the Navier-Stokes equation. The momentum equation is defined in tensor notation as

$$\frac{\partial \rho u_i}{\partial t} + \frac{\partial \rho u_j u_i}{\partial x_j} = -\frac{\partial p}{\partial x_i} + \mu \frac{\partial^2 v_i}{\partial x_j^2} + \rho g_i \tag{3.1}$$

where u is the velocity, ρ the density, p is the pressure, μ the dynamic viscosity and x_i denotes the direction. For multiphase flows the momentum equation is rewritten to account for the multiple phases as follows

$$\frac{\partial}{\partial t}(\rho u_i) + \frac{\partial \rho u_j u_i}{\partial x_j} = \frac{\partial T_i}{\partial x_i} + \rho g_i + f_{i,\sigma} + f_{i,wa} \tag{3.2}$$

where $\frac{\partial T_i}{\partial x_i}$ denotes the momentum transfer between phases, f_σ is the surface tension force at the interface and f_{wa} the wall adhesion force.

3.2 Multiphase Modelling

For tracking the interface between the two fluids the Volume of Fluids (VOF) method (Hirt & Nichols, 1981) is used. The method is considered a direct numerical simulation method for multiphase flow where the interface is resolved for every time step. VOF is based on a colour-function where the volume fraction of each computational cell is tracked directly while solving a single set of momentum equations. Each cell takes value, $0 \leq \alpha_i \leq 1$, that represents the volume fraction of phase i in the cell. $\alpha_i = 1$ means that the cell only contains the phase and $\alpha_i = 0$ none of phase i is present. When α_i is between 0 and 1 the cell contains several phases indicating that the interface between phases is located within the cell.

The single momentum equation can be used as the material properties for cells containing both phases are varied with the volume fraction as

$$a = \alpha a_l + (1 - \alpha) a_g \tag{3.3}$$

where a could be either density, ρ, or stress, T.

The interface is then tracked by solving the transport equation for the volume fraction advection.

$$\frac{\partial \alpha}{\partial t} + \nabla \cdot (\alpha \mathbf{u}) = 0 \tag{3.4}$$

The above equation can be written on full form of the continuity equation for the volume fraction of phase q as

$$\frac{1}{\rho_q}\left[\frac{\partial}{\partial t}(\alpha_q \rho_q) + \nabla \cdot (\alpha_q \rho_q \vec{v}_q) = S_{\alpha_q} + \sum_{p=1}^{n}(\dot{m}_{pq} - \dot{m}_{qp})\right] \tag{3.5}$$

Where $\dot{m}_{qp}$ is the mass transfer from phase q to phase p, and vice versa ("Ansys Theory Guide", 2020). Moreover, S_{α_q} represents a source term.

The continuity equation may be discretized using either an implicit or explicit formulation. For the implicit formulation, the flow variables at the current time step are a function of other quantities at the current time step. For the explicit formulation, the flow quantities are a function of known quantities of a previous time step.

3.2.1 Interface Discretization

Discretization of the interface can be done using algebraic or geometrical reconstruction techniques ("Ansys Theory Guide", 2020). A few commonly used algebraic methods of interface discretization are the donor-acceptor formulation, flux-corrected transport and CICSAM schemes. As an example of the algebraic methods, the CICSAM scheme is given by the following equation.

$$\alpha_f = \alpha_d + \beta \nabla \alpha_d \cdot \overline{dr} \tag{3.6}$$

where α_f and α_d is the face and donor-cell volume fraction respectively and $\overline{dr}$ is the distance between face and cell. The β variable is a slope limiter, which determines the type of spatial discretization used in order to maintain a sharp interface. By changing to a different discretization, it may reduce the occurance of spurious oscillations near sharp interfaces that may occur for higher order spatial discretization schemes.

As for the geometrical reconstruction, the Piecewise Line Interface Calculation (PLIC) is widely used. It defines straight line segments approximating the actual interface between two fluids from the gradient of the volume fraction. This is an improvement from Simple Line Interface Calculation (SLIC) that generates straight lines aligned to the grid. A comparison between the two methods can be seen in Figure 3.1.

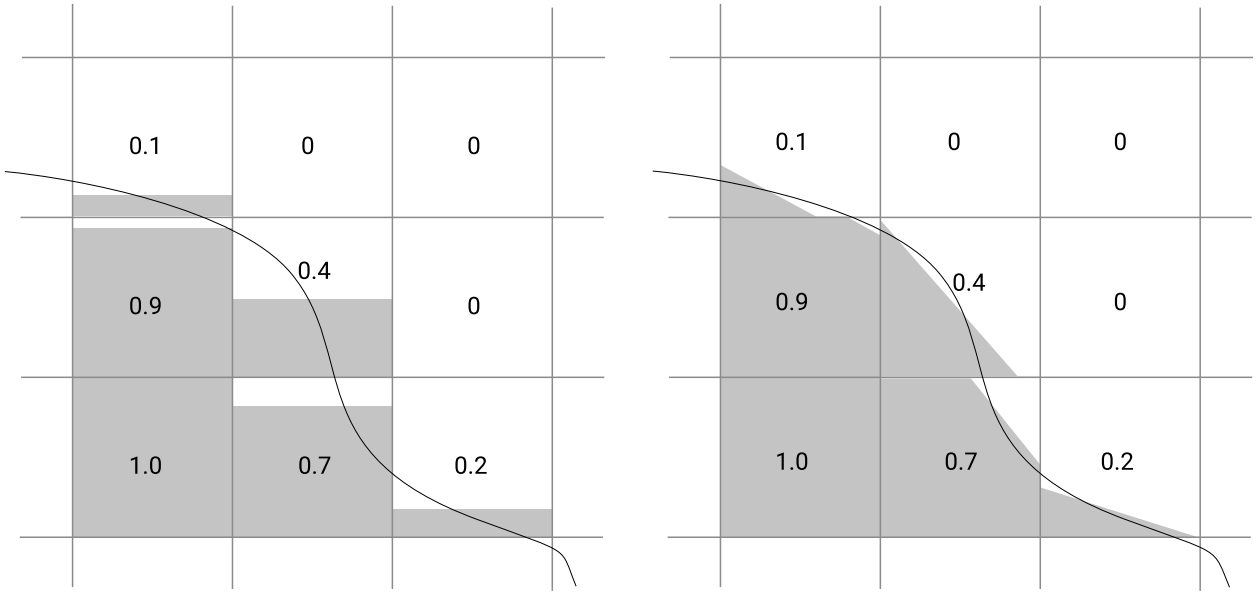

(a) *SLIC* **(b)** *PLIC*

Figure 3.1: *Geometrical reconstruction methods.*

First, the position of the linear interface relative to the center of each partially-filled cell is calculated, according to the SLIC or PLIC methodology presented above. Then, fluid is advected through each face from the velocity distribution on the face and the previously computed linear interface. Lastly, the volume fraction for each cell is calculated from the flux balance calculated in the previous step.

3.3 Wall Boundary Condition

As the droplets move across the solid surface, the contact line moves across a no-slip boundary. This expectedly leads to a stress singularity at the contact line, which stems from the fact that continuum mechanics break down at molecular distances from the contact line (Afkhami et al., 2009). This can be circumvented by modelling the molecular interactions between the fluid and solid phases. Commonly, this is done by allowing for slip or partial-slip along the contact line, as can be seen in Figure 3.2. This relaxes the singularity at the no-slip boundary. The Navier-slip law relates the slip as proportional to the shear stress through the Cauchy stress tensor (Gariboldi & Takahashi, 2019).

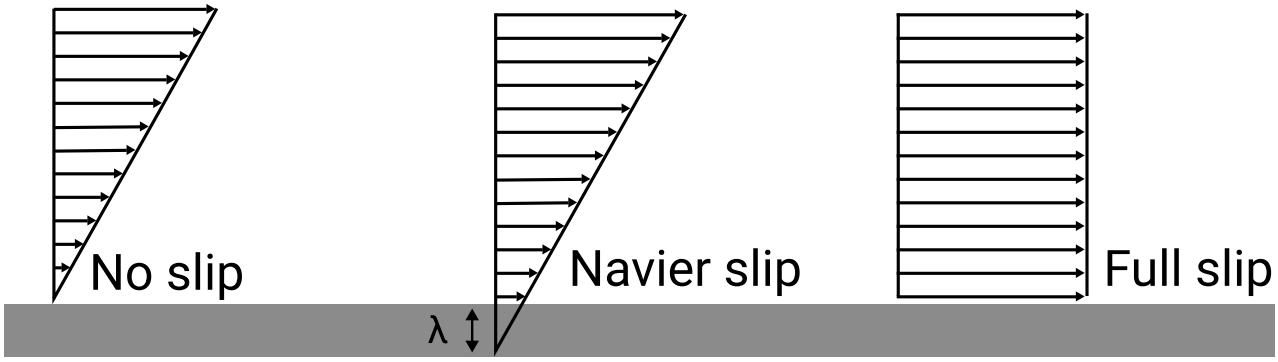

Figure 3.2: *Slip conditions over wall.*

$$\begin{aligned} \sigma(u,p) &= 2\mu D(u) - pI \\ D(u) &= \frac{1}{2}\big(\nabla u + (\nabla u)^T\big) \end{aligned} \tag{3.7}$$

where u and p is the fluid velocity and pressure respectively and I is the identity matrix. This gives the wall velocity as

$$v|_{x=0} - U = \lambda \frac{\partial v}{\partial x}|_{x=0} \tag{3.8}$$

Where v is the velocity at the boundary, U is the velocity of the solid phase and λ is the defined as the slip length, which determines how much the no-slip boundary is relaxed.

It should also be noted that the contact line velocity problems on no-slip walls is limited for coarse grids where the wall region is resolved on a macroscopic level as it introduces a numerical slip that allows for spreading of the contact line on the no-slip boundary (Renardy, Renardy, & Li, 2001). This can be seen as an interpolation of the cell-centered fluid velocity due to numerical diffusion onto the wall surface.

3.4 Surface Tension Force Model

The surface tension and wall adhesion forces can be modelled using the Continuum Surface Force model presented by Brackbill, Kothe, and Zemach (1992). The surface tension force is then approximated as a body force defined as

$$\mathbf{F}_\sigma = \sigma\kappa\nabla\alpha \tag{3.9}$$

where σ is the surface tension coefficient between liquid and gas, and κ is the liquid-gas interface curvature. The surface curvature is given by local gradients of the surface normal that in turn can be defined as the normalised volume fraction gradient.

$$\kappa = \nabla \cdot \hat{n} \tag{3.10}$$

where $\hat{n}$ is the normal of the interface. The normal can in turn be approximated by the normalised volume fraction gradient

$$\hat{n} = \frac{\nabla\alpha}{|\nabla\alpha|} \tag{3.11}$$

In flows where the surface tension is dominate, for example low velocity droplet impingement, the interface curvature approximation can cause problems. This is due to the fact that the curvature is approximated from the volume fraction gradient, and will therefore not be an even field. The local variations in surface tension due to this can form artificial velocity fields that are not physical. These velocity fields are known as parasitic or spurious currents and can give a deformed curvature of the interface.

3.5 Dynamic Contact Angle Models

The contact angle is implemented as boundary conditions at the contact line between the two phases and the wall. For static contact angles this is simply a material property, but the dynamic contact angles vary with variations in viscous and inertial forces. The dynamic contact angle is very complex but there are multiple models based on empirical studies to describe the variations, three of which are described here.

For all models the direction of the contact line velocity is needed. The velocity of the contact line can be determined by the actual cell velocities, where the cell velocity is projected down onto the plane of the wall as

$$V_{cl} = \hat{n}_{wall} \times u_{cell} \times \hat{n}_{wall} \tag{3.12}$$

This is used to determine whether the interface is advancing or receding. The direction is found by the scalar product between the inward directed volume fraction gradient, and the contact line velocity. A negative value gives that the contact line is moving opposite of the volume fraction gradient, yielding an advancing contact line.

$$\mathbf{V}_{cl} \cdot \nabla\alpha \begin{cases} \leq 0: & \text{Advancing} \\ > 0: & \text{Receding} \end{cases} \tag{3.13}$$

3.5.1 Kistler's Model

The dynamic contact angle model presented by Kistler (1993) is a function of contact line velocity, in the form of capillary number, Ca, the static contact angle, θ_E and the inverse of the empirical function of Hoffman (1975), $f_H^{-1}(x)$.

$$\theta_D = f_H(Ca + f_H^{-1}(\theta_E)) \tag{3.14}$$

where Hoffman's empirical equations is defined as

$$f_H(x) = \arccos\left(1 - 2\tanh\left(5.16\left(\frac{x}{1 + 1.31x^{0.99}}\right)^{0.706}\right)\right) \tag{3.15}$$

This model can be considered valid for advancing contact angles but not for receding. As the Kistler model does not account for receding contact angles, this can either be done by setting the receding contact angle as static or introducing another model to be used in conjunction with Kistler's model.

3.5.1.1 Dynamic Receding Contact Angle Model

One possible model for calculating the receding contact angle was introduced by Nichita, Zun, and Thome (2010) where the contact angle can be calculated as

$$\theta_D = (\theta_R^3 - 72Ca)^{1/3} \tag{3.16}$$

The model is based on a correlation presented by Tanner (1979).

3.5.2 Shikhmurzaev's Model

Shikhmurzaev's model (Shikhmurzaev, 2007) gives a relation between the dynamic contact angle, the static contact angle, contact line velocity and some phenomenological constants as

$$\cos(\theta_D) = \cos(\theta_A) - \frac{2u(a_1 + a_2 u_0)}{(1 - a_2)\left((a_1 + u^2)^{1/2} + u\right)} \tag{3.17}$$

where a_1 is given by

$$a_1 = 1 + (1 - a_2)(\cos(\theta_A) - a_4) \tag{3.18}$$

and a_2, a_3, a_4 are fitted parameters from experiments. For the case of water-air systems these parameters are given by Malgarinos, Nikolopoulos, Marengo, Antonini, and Gavaises (2014).

$$a_2 = 0.54, a_3 = 12.5, a_4 = 0.07 \tag{3.19}$$

The radial velocity, denoted as u_0 can be estimated as

$$u_0 = \frac{\sin(\theta_D) - \theta_D \cos(\theta_D)}{\sin(\theta_D)\cos(\theta_D) - \theta_D} \tag{3.20}$$

and u is the dimensionless velocity of the contact line between the two phases and the wall defined by the capillary number as

$$u = a_3 Ca = a_3 \frac{V_{cl}\mu_l}{\sigma_{lg}} \tag{3.21}$$

This model is also valid only for the advancing contact angle, and the receding contact angle model, presented in section 3.5.1.1, can be used together with Shikhmurzaev's model, as with Kistler's model.

3.5.3 Cox's Model

The final model was developed by Cox (1986) and is valid for both advancing and receding contact angle

$$\theta_D = g^{-1}\left(g(\theta_{app}) + Ca \log\left(\frac{L}{\lambda}\right)\right) \tag{3.22}$$

where L is the apparent length and λ is the physical slip length and log is the natural logarithm. θ_{app} is the apparent contact angle and can either be the equilibrium contact angle, θ_E, or the advancing or receding dynamic contact angle respectively. For the latter case, the advancing and receding contact angles has to be calculated from the equilibrium contact angle and capillary number from empirical correlations which has not been analysed in this study. Therefore, the equilibrium contact angle may be used. To differentiate the receding and advancing equations, the receding contact angle is calculated using a negative contact line velocity to ensure that the contact angle is minimised with increase in velocity.

For water-air systems where the surrounding fluid is of much smaller viscosity the function $g(\theta)$ can be simplified to

$$g(\theta) = \int_0^\theta \frac{x - \sin x \cos x}{2 \sin x} dx \tag{3.23}$$

Several studies (Göhl et al., 2018; Dupont & Legendre, 2010; Legendre & Maglio, 2015) have further simplified the g-function by approximating both the function and its inverse as polynomials first proposed by Mathieu (2003)

$$\begin{aligned} g(x) &\approx x^3/9 - 0.00183985x^{4.5} + 1.845823 \cdot 10^{-6} \cdot x^{12.258487} \\ g^{-1}(x) &\approx (9x)^{1/3} + 0.0727387x - 0.0515388x^2 + 0.00341336x^3 \end{aligned} \tag{3.24}$$

3.5.4 Quasi-Dynamic Contact Angle Model

In addition to the true dynamic contact angle models presented above, there are also quasi-dynamic contact angle models. These are a more basic approach to modelling the dynamic contact angle and is solely based on whether or not the contact line is advancing or receding (Göhl et al., 2018). Just like in the other models the dynamic contact angle is imposed as a boundary condition on the wall. However, instead of calculating the dynamic contact angle, it is set constantly as equal to an advancing contact angle for a spreading motion and to a receding contact angle if the liquid is receding.

$$\theta_D = \begin{cases} \theta_A & : \text{Advancing contact line} \\ \theta_R & : \text{Receding contact line} \end{cases} \tag{3.25}$$

This means that the hysteresis of the contact angle is taken into consideration, even though the actual spread is not. This model is therefore highly dependent on whether or not there is experimental data of contact angle hysteresis available. If there is no experimental data, the model is reduced to a static model, where $\theta_D = \theta_E$.

4 Methods

This chapter handles the methodology used for implementation of the previously described numerical models, in Section 3, and simulations of water droplet impingement and water film spread using said models. The chapter also describes the validation processes for the implemented dynamic contact angle models using convergence studies and experimental data.

4.1 Implementation

This section describes the implementation of static and dynamic contact angle models into commercial software ANSYS Fluent. In ANSYS Fluent, the static contact angle can be set in the graphical user interface as a boundary condition to the continuum surface force method. The implementation of a dynamic contact angle model is done through user defined functions that are based on the implementation of static contact angles, with the addition of contact line velocity and direction estimations.

4.1.1 Static Contact Angle

As previously mentioned, when wall adhesion effects are turned on, the static contact angle can be set as a boundary condition directly in the ANSYS Fluent graphical user interface. In equilibrium, the wall adhesion can be easily estimated through the Continuum Surface Force model framework, described in Section 3.4. In this case the static contact angle is used to impose the boundary condition instead of imposing it at the wall itself, ("Ansys Theory Guide", 2020). The contact angle will adjust the surface normal and curvature in cells near the wall as

$$\hat{\mathbf{n}} = \hat{\mathbf{n}}_w \cos\theta_E + \hat{\mathbf{t}}_w \sin\theta_E \tag{4.1}$$

where θ_E is the equilibrium contact angle and $\hat{\mathbf{n}}_w$ and $\hat{\mathbf{t}}_w$ are the normal and tangential unit vectors to the wall, respectively.

By combining the contact angle and the normally calculated surface normal in the near-wall cell region, the local curvature of the surface can be determined. This curvature is then used to adjust the body force term in the surface tension calculation.

4.1.2 Dynamic Contact Angle

The dynamic contact angle model is implemented as a user defined function, UDF, which is coupled, or hooked, into the graphical user interface. Using this methodology, a more advanced function may be written and set as a boundary condition, in the same way as for the static contact angle.

The user defined function is constructed using a variation of macros. The main macro used is the Define Adjust macro, which functions on a domain level and is executed at every iteration before transport equations are solved ("Ansys Fluent Customization Manual", 2020). For this case the Define Adjust macro is used to calculate and store the dynamic contact angle for every wall cell. Storage of variables is handled using User Defined Memory, UDM, which allows for allocation of variables within the User Defined Function. Figure 4.1 shows a flowchart of what is done within in the Define Adjust macro, the numerical procedure of the function is described in detail in Section 3.5. The models used to calculate the contact angle are Kistler's model for the advancing contact angle and Dynamic receding contact angle model for the receding. The choice of models was done arbitrarily as all the models can be implemented in a similar fashion generating fairly similar results. If the UDF is supposed to be used for a specific case where one of the models would be more suitable, it would be an easy change as the main code would stay the same and only the contact angle equations would change.

Additionally, the Define Profile macro is used to define a custom boundary condition which varies as a function of spatial coordinates and time. The Define Profile macro reads the stored dynamic contact angles from the UDM and is coupled into the ANSYS Fluent graphical user interface where the otherwise static contact angle is defined and therefore replacing it with the dynamic contact angle.

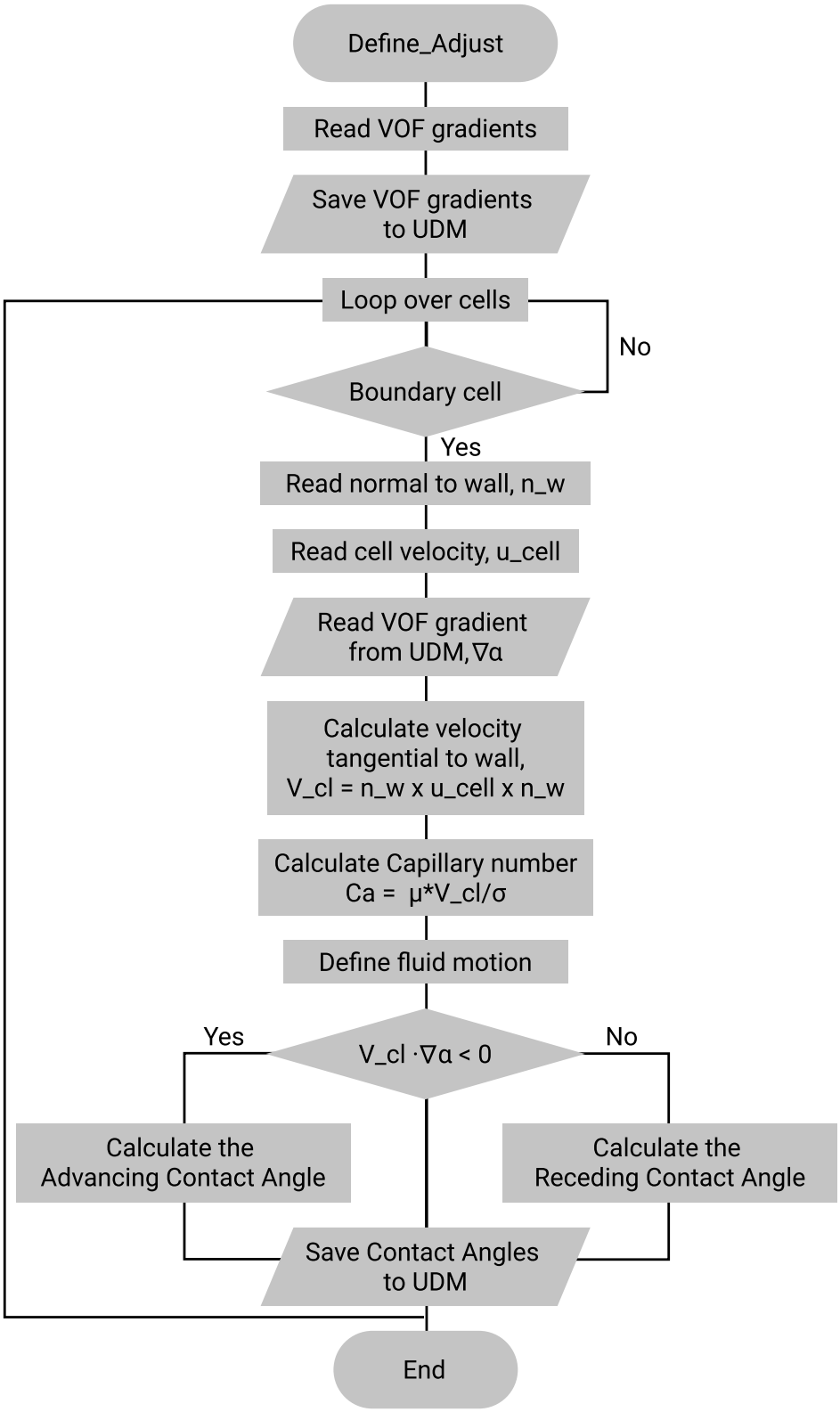

Figure 4.1: *Flowchart of the function within the Define Adjust macro of UDF.*

4.1.3 Wall Boundary Conditions

The wall boundary condition is by default set to no-slip, as previously explained, this will cause high stresses along the wall. The effects of relaxing the no-slip boundary using a Navier-slip boundary condition is therefore introduced to enable to the droplet to slip along the surface, with a velocity which is proportional to the velocity gradient over the wall, and the slip length, λ. For all cases, this slip length was set to the distance to the centroid of the near-wall cells. The slip length is approximately half the height of the first cell height, which may be seen in Tables 4.3, 4.4 and 4.8 for the plane and inclined droplet impingement and water film cases, respectively.

4.2 Simulation

This section handles the set up of all conducted simulations, including droplet impingement onto plane and inclined surfaces, as well as water film evolution over part of an Ericsson 5G-radome. The drop impingement simulations are based on experimental set up as to validate the data whereas the water film simulations are not validated but was rather done as a proof-of-concept in order to test the models stability for larger amount of water and over complex domains. All needed data for the simulations are presented below as well as all settings and methods used for the simulations.

Simulations are performed in three dimensions with a computational domain specific to the case in question. The domain consists of air and a water droplet where properties of the air and water are specified in Table 4.1.

Table 4.1: Physical properties of water drop used in convergence studies.

Fluid	Density $[kg/m^3]$	Viscosity $[Pa \cdot s]$	Surface Tension $[N/m]$
Water	998	0.001003	0.0728
Air	1.225	1.7894e-5	-

General for all cases is that the impacting wall is set to a no-slip boundary with a specified contact angle, either static or dynamic, all other boundaries are set to pressure outlet. For each case, a simulation using the dynamic contact angle and a Navier-slip boundary condition has also been performed and are compared to the no-slip simulations. Further the meshing is described in Section 4.3.1.

To compare simulated results to experimental data and for the convergence study the spread and height factors β and ξ are used. Spread factor is defined as the diameter of the wetted area, d, divided by the initial diameter of the droplet D_0

$$\beta = \frac{d}{D_0} \tag{4.2}$$

In the same way the height factor is defined as the maximum height of the drop, h, divided by the initial diameter of the droplet D_0

$$\xi = \frac{h}{D_0} \tag{4.3}$$

The value of the diameter and height is taken as the measurement of the $\alpha = 0.5$ iso-surface. So, the measurement is taken for one side of the drop where the volume fraction is 0.5 to the other side at the point where $\alpha = 0.5$. For the height the measurement is taken from the wall until the highest point where $\alpha = 0.5$.

4.2.1 Plane Droplet Impingement

Droplet impingement onto a plane surface is done for a variation of Weber numbers onto both a glass and wax surface, which is hydrophilic and hydrophobic respectively, see Table 4.2. To evaluate the validity of the simulated results, the spread factor evaluation is compared to experimental data from Rioboo, Marengo, and Tropea (2002). This is done for all cases described below in Table 4.3. In addition to the dynamic contact angle simulations, simulations using a static contact angle are performed and compared. For these simulations,

the equilibrium contact angle is used.

Table 4.2: Advancing and receding contact angles on the two different surfaces used for droplet impact.

Surface	Contact angles $[\theta_A - \theta_E - \theta_R]$
Wax	$105 - 100° - 95°$
Glass	$15 - 10° - 6°$

The domain used for the simulations is a cylinder with varying base diameter and height depending on the surface and Weber number due to expected variance in spread and height. A water droplet is patched into the domain, just above the impinging surface, with a diameter and velocity that matches that of the Rioboo et al. (2002) experiments. The domain and droplet data for each case is described in Table 4.3

Table 4.3: Domain and droplet data for simulations of droplet impingement onto a plane surface.

Case	Surface	Drop diameter [mm]	Velocity [m/s]	Weber number [-]	Domain diameter [mm]	Domain height [mm]
1	Wax	2.75	1.18	52	12	10
2	Wax	3.17	3.6	563	20	6
3	Glass	3.04	1.18	58	16	6
4	Glass	3.17	3.6	563	20	4.5

To evaluate the occurrence of turbulence the drop Reynolds number can be calculated as

$$Re_d = \frac{\rho_g U D_0}{\mu_g} \approx 781.25 \tag{4.4}$$

where the data from case 2 has been used. There is no direct limit that determines when the flow turns turbulent, but the low number would indicate that the drop impingement can be considered laminar.

The simulations are run until sufficient amounts of data is collected to give a fair comparison to the experiments, which is around 30 ms for all cases. For Case 1, the static and dynamic contact angle models are compared in depth. For this comparison the simulations are run for close to 130 ms, as to catch the moment when the droplet enter equilibrium.

4.2.2 Inclined Droplet Impingement

Impingement onto inclined planes are done, in a similar fashion to the plane impingement, for a variation of inclinations, Weber numbers and for both glass and wax surfaces, see Table 4.4. The simulated results are then compared to experimental values from Šikalo, Tropea, and Ganić (2005). The advancing and receding contact angles which are used in the simulations are the same as for plane impingement and can be seen in Table 4.2.

Different domains are used for the different inclinations as the droplet spread is dependent on the inclination, φ. The inclination of the plane is defined as is shown in Figure 4.2. The dimensions of each domain is defined in Table 4.4. As in the case of plane impingement, a water droplet is patched into domain just above the impinging surface with a diameter and velocity that matches that of the experimental set up by Šikalo, Tropea, and Ganić (2005). For all inclined simulations, the droplet diameter is set to 2.7mm. The impingement velocity is set to 1.16 m/s or 3.25 m/s, corresponding to Weber numbers of 50 and 391, respectively. A no-slip boundary condition is used for the impingement surface. Simulations are also run using a Navier-slip boundary condition for the inclined surfaces, as described in Section 3.3. These simulations are purely run together with the dynamic contact angle formulation and not for static contact angles.

Table 4.4: Domain and droplet data for simulations of droplet impingement onto an inclined surface

Case	Angle $\varphi[^\circ]$	Surface	Domain length [mm]	Domain width [mm]
5	45	Wax	30	30
6	45	Glass	30	30
7	80	Wax	35	12
8	80	Glass	35	12

All simulations of droplet impingement onto inclined surfaces, are run sufficiently long to compare with the experimental data. In order to measure the distortion of droplets upon impingement on inclined surfaces, the spreading of droplets from the moment of impact were measured. The spread factor of a droplet impinging on an inclined surface may be described relative to the original point of impact using a frontal part, x_{front}, defined as the length of the droplet in front of the point of impact. There is also a rear part, x_{rear}, which is defined as the length of the droplet behind the point of impact. As the two different lengths are defined relative to the point of impact, they are allowed to become negative. This happens for cases where the rear droplet interface slides past the point of impact. Depending on the wettability of the impact, the spread factor will develop differently. The back edge may spread backwards in the case of high wettability, or slip forwards, down the plane, in the case of low wettability. Depending on Weber number, the droplet may show very different behaviours during impact. For low Weber number impingements, the droplet may rebound off the surface without any significant wetting. Increasing the Weber number may lead to splashing and/or lamellar spread. In these cases all the lamella are treated as a separate when measuring the spread factors, meaning that the both the front and rear spread is measured for the lamella with the furthest spread. Furthermore, only the volume fraction of water which is in contact with the wall is used to measure the spread factor, and any small droplets which are launched away by the impact are neglected.

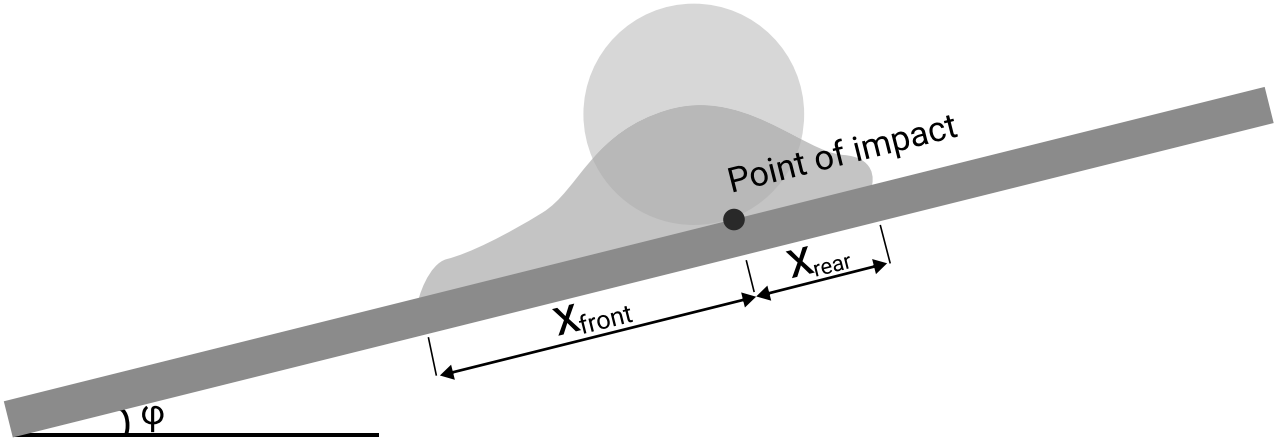

Figure 4.2: *Spread factor of inclined droplet impingement.*

4.2.3 Water Film

In order to evaluate how the dynamic contact angle model handles more complex geometries, as well as geometries with different hydrophobicities for different areas, simulations are run on a domain representing an Ericsson 5G radome, which can be seen in Figure 4.3.

The radome has a height of approximately 32 cm, and its width measures 36.5 cm. Due to this size, a small region of the radome is used to simulate the water flow. The region of interest is on the slanted side of the radome, as this region contains a small window through which the microwave radiation is emitted. The geometry was simplified using ANSYS SpaceClaim Design Manager in order to remove the smallest radii in the domain to simplify meshing.

The simulation domain can be seen in Figure 4.3. An inlet can be seen at the top of the domain, coloured in

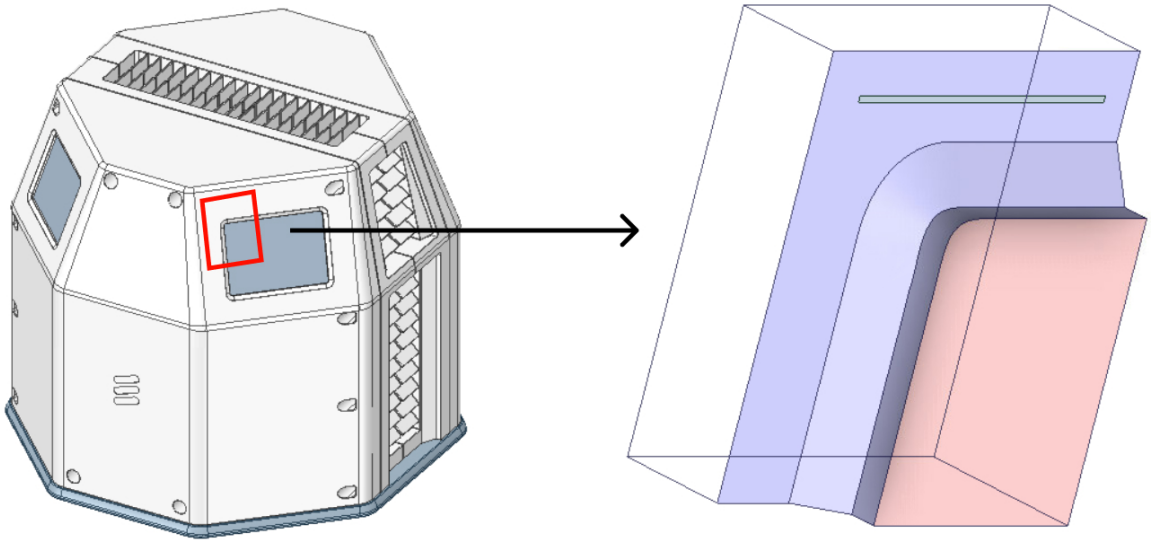

Figure 4.3: *Ericsson 5G radome simulation domain.*

green. The radome window is coloured in red, and the remainder of the surface is coloured in blue. Water enters the domain through the slit measuring 24x0.5 mm at the top of the domain, which is defined using a mass flow inlet boundary condition with a mass flux of 100 $\frac{kg}{m^2 s}$ normal to the inlet. The water is then allowed to flow down the radome which is defined using wall boundary conditions with separate dynamic contact angles for the window and the remainder of the surfaces. Both the mass flux and the hydrophobicity of the surfaces is chosen arbitrarily, as no appropriate experimental results was found for validation. The defined contact angles can be seen in Table 4.5.

Table 4.5: Advancing and receding contact angles on the two different surfaces on the radome surface

Surface	Contact angles $[\theta_A - \theta_E - \theta_R]$
Wall	$95° - 90° - 85°$
Window	$35° - 30° - 25°$

The simulation was also run using static contact angles for comparison. For the static contact angles, θ_E in Table 4.5 were used.

4.2.4 Solution Methods

The simulations are set up using an explicit Volume of Fluid method, as the explicit formulation has an advantage in numerical accuracy compared to the implicit formulation ("Ansys User Guide", 2020). The time step size is however more limited in the explicit formulation, meaning longer simulation times.

The spatial discretization is divided into pressure, gradient and momentum, for these the PRESTO!, Least squares cell based and Second order upwind methods are used, respectively. For the Volume of Fluid method a scheme for the volume fraction interpolation is also needed. For this a geometrical reconstruction scheme, Piecewise Line Interface Calculation, PLIC, as described in Section 3.2 is used instead of an algebraic alternative as the accuracy is higher with geometrical reconstruction ("Ansys User Guide", 2020).

The simulations are set up with the Pressure-Implicit with Splitting of Operators, also known as PISO, scheme for pressure-velocity coupling where the neighbour correction is set to 3. The scheme is chosen as it is what ANSYS suggests for transient problems as the number of iterations can be greatly reduced ("Ansys Theory Guide", 2020).

For the time discretization a first order implicit formulation was used, as the higher order schemes are not available for the explicit VOF method. Furthermore, the option in ANSYS Fluent of using a non-iterative time advancement (NITA) method was chosen, as it requires a considerably less amount of computational effort than the iterative time-advancement scheme. The non-iterative time-advancement scheme does not perform the outer iterations for each time-step, as the splitting error does not need to be reduced to zero, but it is sufficient for it to have the same order as the truncation error ("Ansys Theory Guide", 2020). The NITA scheme does however allow for inner iterations to solve the individual set of equations.

The time stepping is determined through the Courant number, also known as CFL. The idea behind the Courant number is that, for a fluid flowing over a discrete spatial grid the flow cannot travel to adjacent grid points in a single time step and give an accurate solution. The Courant number is therefore designed to limit the travel, so for a Courant number < 1 the fluid will remain within one grid cell over the time step. By setting a constant Courant number, the time step is adaptive and will set to what is necessary to fulfill the Courant requirement for the given grid, a decrease in Courant will therefore result in a decreased time step. To allow for the Courant number to be within an acceptable range, the minimum timestep size has to be set to $1e-8$.

4.3 Convergence Study

To evaluate the dependence of mesh and time step of the implemented dynamic contact angle simulation a grid and Courant-number convergence study has been conducted. The spread and height factors of a water droplet impingement on plane and inclined surfaces. A smaller mesh study was also done for the water film simulation.

4.3.1 Mesh Convergence Plane Impingement

The spread and height factor evolution over time is compared for a variation of meshes where the overall cell size is reduced. For the simulations, a cylindrical domain as described for Case 1 in Section 4.2.1, i.e low Weber-number impingement onto a hydrophobic surface, is used. The simulations are run until 23 ms is reached, which represents the moment right before a drop is detached due to jet spreading phenomena. The mesh is polyhedral with two variations of near-wall refinement. The first variation uses 5 prism layers, i.e a layer of orthogonal prismatic cells, smoothly transitioning from the impacting wall with a transition rate for 0.272 and a growth rate of 1.2. The prism layers are generally used to minimize the height of the cells closest to the wall to achieve a Y+ value lower than one, which is desirable for turbulence resolution. For this case the refinement and prism layers were introduced as to maximize the number of cell for resolving the water film at its thinnest areas. The second type of refinement is done by simply refining the polyhedral cells close to the wall.

The overall mesh is set to be so that the number of cells over the original diameter of the drop is varied between approximately 15 and 35 as presented in Table 4.6. In the table the first cell height is also presented as it is of importance for the slip (Afkhami et al., 2009; Renardy et al., 2001). For all simulations in the mesh convergence study the time step is set to be adaptive with a constant Courant number of 0.2.

Table 4.6: Numerical parameters of grid convergence study for a hydrophobic surface.

Mesh no	Cells/D_0	Total cell count	First cell height [m]	Near wall refinement
1	approx. 15	252 000	8.81 e -6	Prism layer
2	approx. 20	472 000	7.09 e -6	Prism layer
3	approx. 25	854 000	5.89 e -6	Prism layer
4	approx. 35	1 590 000	4.5 e -6	Prism layer
5	approx. 23	815 000	9.10 e-6	Polyhedral refinement
6	approx. 30	1 290 000	6.74 e-6	Polyhedral refinement
7	approx. 35	2 530 000	3.38 e-6	Polyhedral refinement

4.3.2 Time Convergence

For the time convergence the same domain, droplet diameter and impact velocity is used as for the mesh convergence. An adaptive time stepping is used with four different fixed Courant numbers is tried, CFL = 0.75, CFL = 0.5, CFL = 0.2 and CFL = 0.1, giving increasingly smaller time step lengths. The mesh used for the time convergence test is mesh number 3 from the mesh study and has about 854 000 number of cells with 5 prism layers at the impacting wall.

4.3.3 Mesh Convergence Inclined Surface

The front and rear spread factor evolution over time is compared for three different grids where the overall cell size is reduced between them. Here the $We = 50$, 45° and 80° hydrophobic inclined droplet cases were used. For the simulations, a box-shaped domain as described for Cases 5 and 6 in Table 4.4 is used. The mesh is constructed using polyhedral cells with 5 prism layers. The prism layer is defined as smoothly transitioning from the impacting wall, using a transition rate of 0.272 and a growth rate of 1.2.

The mesh above the prism layer is set to be so that the number of cells over the original diameter of the drop is varied between approximately 10 and 20 as presented in Table 4.7.

Table 4.7: Numerical parameters of inclined droplet impingement grid convergence study.

Mesh no	φ	Cells/D_0	Total cell count	First cell height [m]
1	45°	approx. 10	602 000	9.37 e -6
2	45°	approx. 14	1 160 000	5.09 e -6
3	45°	approx. 20	1 649 000	4.26 e -6
4	80°	approx. 10	714 000	9.36 e -6
5	80°	approx. 14	1 117 000	3.62 e -6
6	80°	approx. 21	1 722 000	2.85 e -6

4.3.4 Mesh Convergence Wall Film

The water film simulation is performed on three different meshes, which can be seen in Table 4.8. For mesh number one, the prism layer is defined as smoothly transitioning with 5 layers from the wall surfaces, using a transition rate of 0.272 and a growth rate of 1.2. For the meshes using polyhedral refinement, local refinement was conducted near the walls.

Table 4.8: Mesh parameters for wall film simulation.

Mesh no	Total cell count	First cell height	Near wall refinement
1	1 678 000	4.04 e -5	Prism layer
2	1 549 000	7.90 e -6	Polyhedral refinement
3	2 009 000	5.94 e -6	Polyhedral refinement

5 Results and Discussion

This chapter presents and discusses the results of all simulations described in Chapter 4, the convergence study and validation of both plane and inclined droplet impingement to experimental data. Furthermore, the more general results of a water film simulation is presented.

Figure 5.1 shows the regime map for droplet impingement. Cases 1-4 denote the plane droplet impingement cases as can be seen in Table 4.3 and Cases 5-8 denote the inclined droplet impingement cases, seen in Table 4.4. As can be seen, the droplet impingement for all plane and inclined surface cases are within regime I. Initially the spread is therefore dominated by inertia and viscous forces can be neglected.

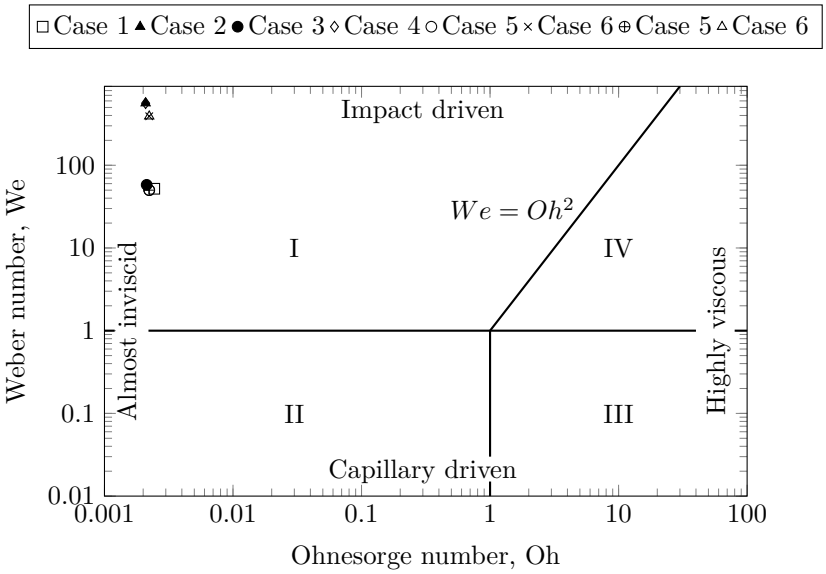

Figure 5.1: *Regime map for droplet spreading. Redrawn from Schiaffino and Sonin (1997).*

5.1 Convergence Study

This section contains the result and discussion about the mesh and time convergence study conducted for droplet impingement onto a hydrophobic surface at $We = 52$, and a mesh convergence study conducted for 45° and 80° inclined droplet impingement onto a hydrophobic surface at $We = 50$.

5.1.1 Mesh Convergence Plane Impingement

A comparison between the two boundary layer refinement approaches can be seen in Figures 5.2 and 5.3. The spread starts off similarly, then the prism layer simulation starts spreading as expected according to the experimental results from Rioboo et al. (2002), whereas the refined near-wall cell simulation is spreading in a square formation and the water is collecting at the corner. When receding, the prism layer droplet creates an upwards motion which results in a jet with droplet detachment, also seen in the experiments (Rioboo et al., 2002). For the refined near-wall cell mesh the receding is slower for the water filled corners as can be seen in Figure 5.3c, leaving tails diagonally from the corners. The receding of the droplet gives it an upward motion, just not as energetic as for the prism layer mesh. Therefore leaving a lower and wider droplet close to the surface, this can clearly be seen in Figures 5.4b and 5.5b.

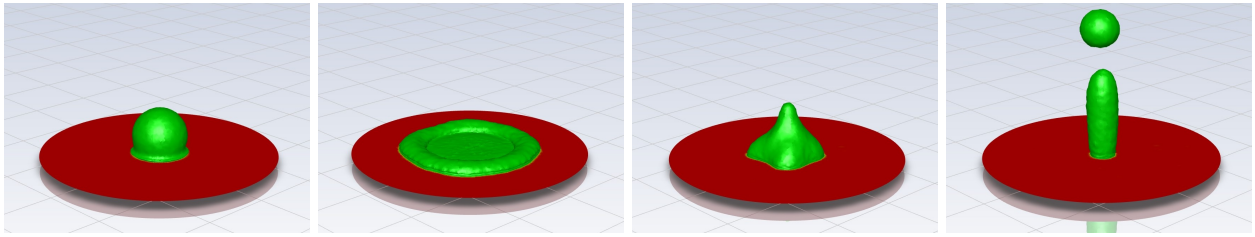

(a) *0.5 ms* **(b)** *6 ms* **(c)** *11 ms* **(d)** *25 ms*

Figure 5.2: *Iso-surface plot of droplet spread evolution for* $\alpha = 0.5$*,* $We = 52$ *and polyhedral mesh with prism layers.*

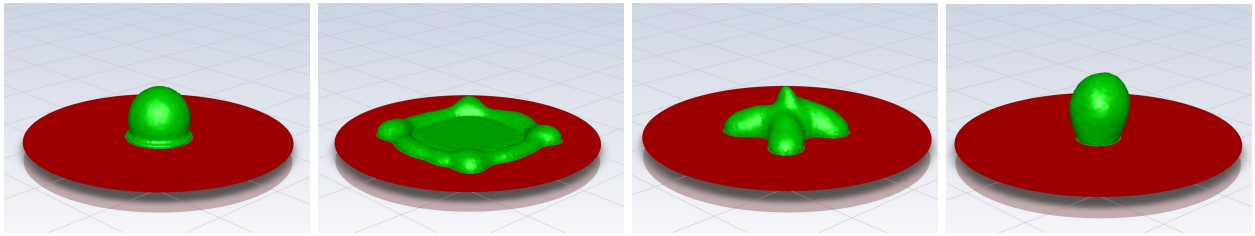

(a) *0.5 ms* **(b)** *6 ms* **(c)** *11 ms* **(d)** *25 ms*

Figure 5.3: *Iso-surface plot of droplet spread evolution for* $\alpha = 0.5$*,* $We = 52$ *and polyhedral mesh with refined near-wall cells.*

The polyhedral mesh with refined near-wall cells needs further work in order to break the symmetry seen in the spreading. A possible solution that could be tested for further development of the dynamic contact angle UDF would be to vary the equilibrium contact angle over the surface as could be the case when the surface is subjected to contamination and weathering. This can be done using the equilibrium contact angle as a mean with a standard deviation as suggested by Meredith, Heather, De Vries, and Xin (2011). This would hopefully give rise to non-uniform flow and would break the symmetric spread pattern.

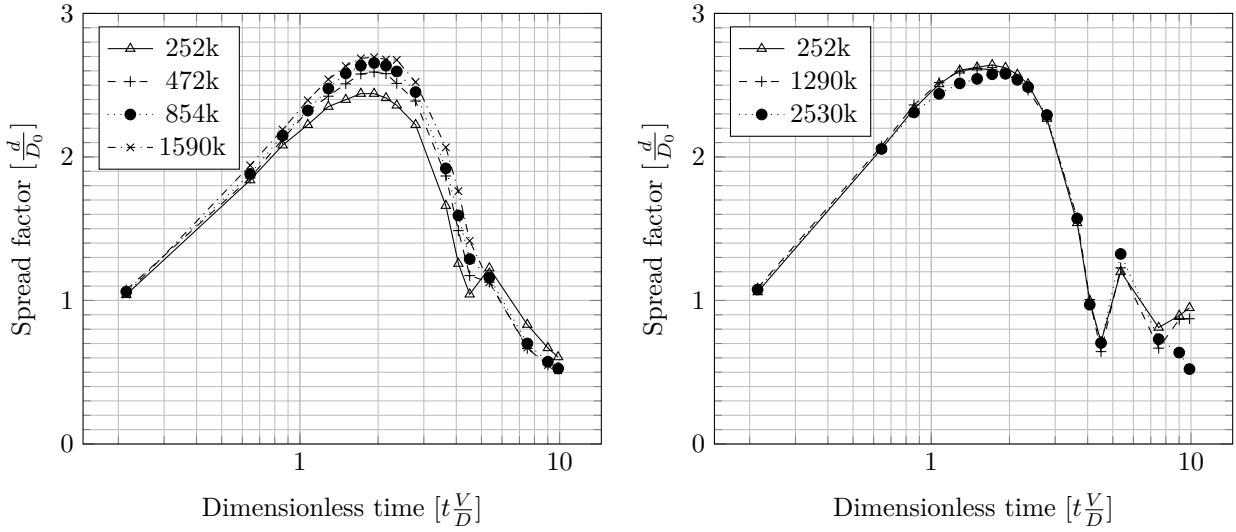

(a) *Polyhedral mesh with Prism layers* **(b)** *Polyhedral mesh with refined near-wall cells*

Figure 5.4: *Spread factor mesh convergence results for a variation of meshes for a cylindrical domain. The refinement in Figure (a) is done with prism layers and (b) by refined near wall cells.*

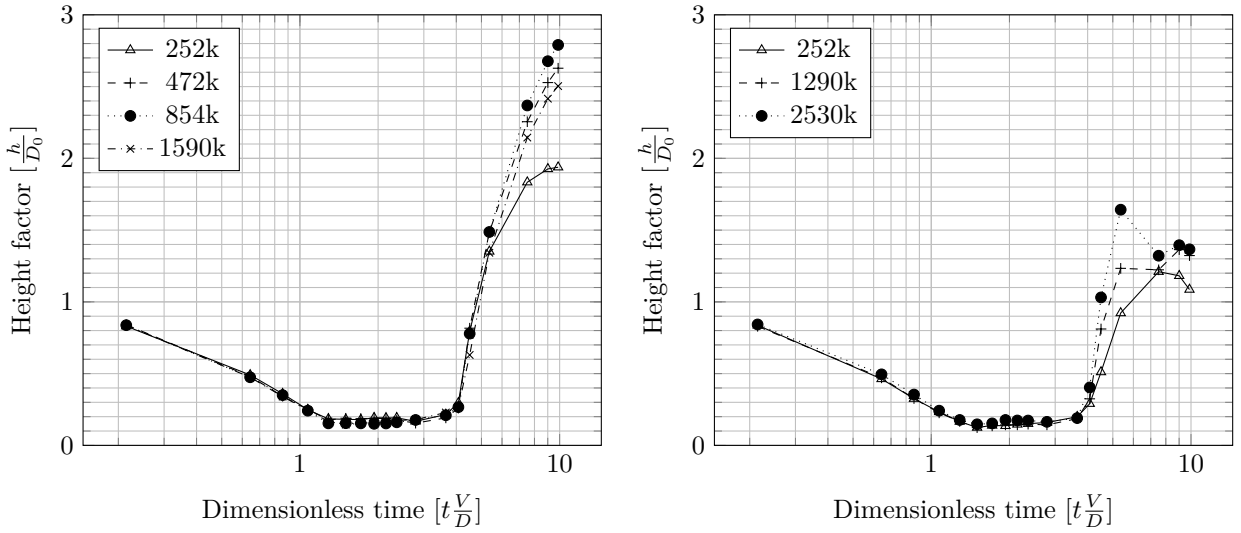

(a) *Polyhedral cells with prism layers* **(b)** *Polyhedral mesh with refined near-wall cell*

Figure 5.5: *Height factor mesh convergence results for a variation of meshes for a cylindrical domain. The refinement in Figure (a) is done with prism layers and (b) by refined near wall cells.*

Figure 5.4 and 5.5 shows the spread and height factor evolution for all mesh versions. It can be seen that the result depends on the mesh although there is convergence. The spread and height factors vary, but the solution is converging with the increase of cells for the prism layer meshes. All three of the finer prism layer meshes also give a spread evolution resembling that shown in Figure 5.2d, and therefore the experiments, suggesting that they are converging towards a correct solution.

An interesting observation is however what can be seen with the height factor. For the finest mesh the height factor is lower than for the other two meshes. A possible explanation for this could be that a finer grid will increase the occurrence of parasitic currents. This causes the velocity of the interface to drastically vary causing deformations and will affect the energy needed for the jet to rise. It is important to note that the change in width and height of the boundary layer cells is not varied at the same rate due to the prism layer approach. This could affect the results of the mesh study, but should not result in the decrease in height seen for the finest mesh.

The coarsest prism layer mesh, in the figure denoted '252k', gives a result that does not resolve the physics as it should as there is no droplet detachment from the jet that bounces off the surface as the experiments show. This explains the much lower height, and higher diameter spread towards the end of the simulation for this mesh. The droplet spread for this mesh is more like the one seen for the mesh with refined polyhedral cells in the near-wall region, although without the symmetrical shape. The drop spreads circularly and recedes only to get a lower rebound than the jet.

From these observations it has been found that the polyhedral mesh with prism layers is the best approach to simulate impingement accurately at this point. For further simulations of droplet impingement onto plane surfaces, a polyhedral mesh with 5 prism layers smoothly transitioning from the impacting wall with a transition rate for 0.272 and a growth rate of 1.2 has been used. The mesh sizing was configured so that for each case it corresponds to the resolution of mesh number 3 in Table 4.6, i.e. a droplet resolution of about 25 cells over the diameter before impact and a first cell height of around 6 micrometers. With this resolution the thinnest part of the drop while spreading is resolved with a minimum of 5 cells.

5.1.2 Time Convergence Plane Impingement

Time convergence was evaluated for a mesh with 5 prism layers and a droplet resolution of 25 cells over the diameter, as previously described. The four different CFL-numbers all give good convergence as can be seen in Figure 5.6. The overall spread convergence is good for all CFL-numbers. However, some differences are

observed in height factor evolution, for the two higher CFL-numbers. This means that a CFL of 0.2 can be considered suitable, as it is converges for both spread and height.

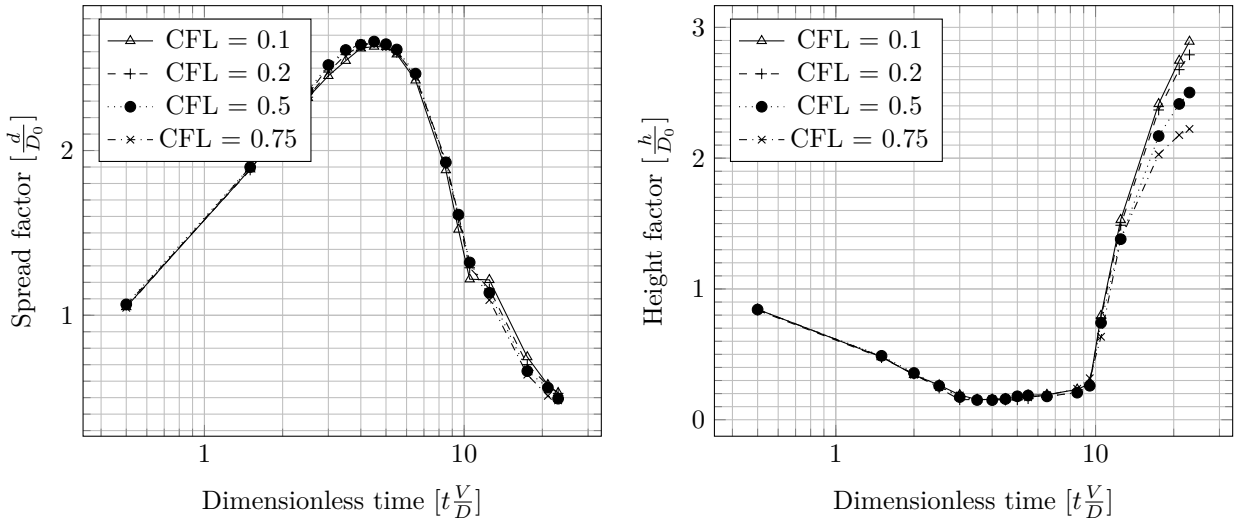

Figure 5.6: *Time convergence study results for four constant CFL-numbers.*

5.1.3 Mesh Convergence Inclined Impingement

Mesh convergence was evaluated for 45° and 80° inclined droplet impingement at $We = 50$ onto a hydrophobic wax surface for a variation of grid resolutions as stated in Table 4.7. Both simulations were run using $CFL = 0.2$. Results are presented as frontal and rear spread factor, x_{front} and x_{rear}, respectively. For both impingement cases, shown in Figures 5.7a and 5.7b, the results are severely lacking when using the coarsest meshes. For these coarse meshes, the frontal spread factor is significantly overpredicted for both cases, and the rear spread factor is significantly under-predicted. This is due to the fact that for this coarse mesh, capturing the expected rebound of the droplet is not possible, and the droplet instead deposits onto the surface. Both the medium grid resolutions and fine grid resolutions accurately predict the expected rebound. This may be due to the fact that the medium and fine grids are able to capture a small air film between the droplet and the surface which acts as a barrier to deposition, as is stated by Šikalo, Tropea, and Ganić (2005).

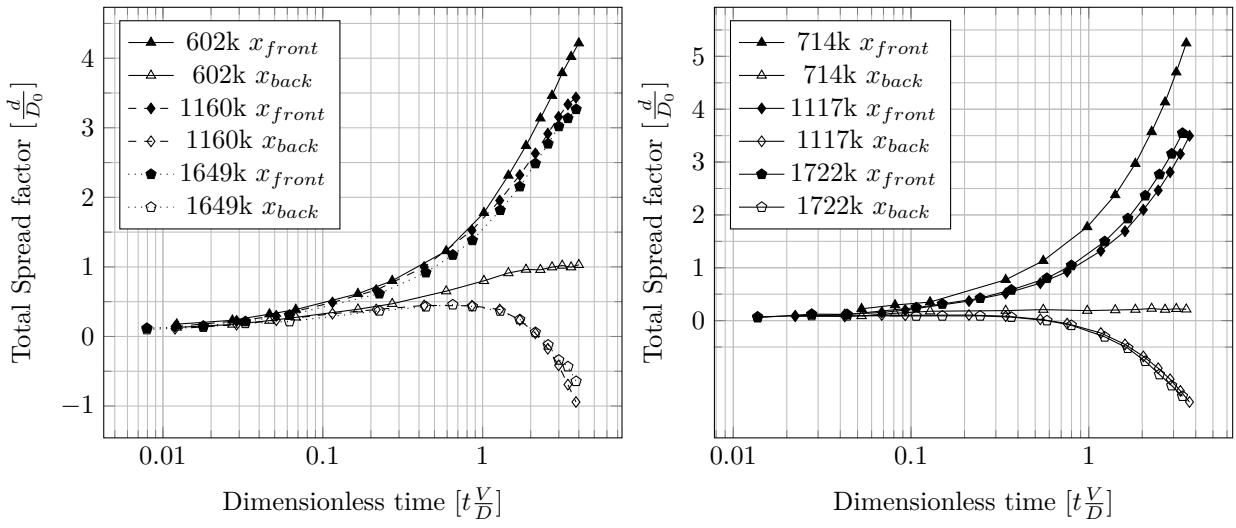

(a) $\varphi = 45°$ **(b)** $\varphi = 80°$

Figure 5.7: *Mesh convergence study results for three different meshes of a inclined box-shaped domain.*

As the medium meshes only show very slight differences from the finer meshes, the results are considered mesh converged. For further simulations of inclined droplet impingement, a polyhedral mesh with 5 prism layers smoothly transitioning from the impacting wall with a transition rate of 0.272 and a growth rate of 1.2 has been used. The mesh sizing was configured such that for each case it corresponds to the resolution of mesh number 2 and 5 in Table 4.7, for the 45° and 80° inclinations, respectively. This yields a first cell height of around 4-5 micrometers and a droplet resolution of about 14 cells over the diameter before impact. The overall mesh is therefore coarser than for the plane impingement as the spread of the inclined impingement does not result in a bouncing or jet effect where the droplet interface has to be resolved far from the wall. The droplet is instead spreading in a lamellar fashion, breaking into smaller droplets on the surface which require a higher resolution on the wall, therefore the first cell height is less for the inclined simulations.

5.1.4 Mesh Convergence Wall Film

Water film simulations were run on three different meshes, as previously described. For both the polyhedral mesh with boundary layer refinement, and the coarser mesh using local refinement, the solution diverged as the water reached the second edge of the wall surface. This result was avoided for the finer mesh, water passed all the edges without diverging. All simulations were run using a Courant number of 0.2. Tests were made where the Courant number was decreased, but this had no improvement on the divergence of the coarser meshes, indicating that the wall film is highly dependent on the choice of mesh resolution.

For the polyhedral mesh with prism layers, mesh number 1 in Table 4.8, the near-wall cells had a very high aspect ratio, approximately 30. Efforts to reduce this aspect ratio were made, but resulted in a massive increase in cell count, significantly increasing computational time. The effect of having high aspect ratio cells near the wall is to significantly reduce the resolution of the mesh in the flow direction of the wall film. This reduction in resolution is likely why the divergence occurred.

For the coarse and fine polyhedral meshes with local refinement, meshes number 2 and 3 in 4.8, the first cell heights were $7.9e-6$ and $5.94e-6$, respectively. This is in the same order as the plane and inclined droplet impingement cases. However, the coarse mesh had a first cell height which is very close to the coarsest meshes in the plane and inclined droplet impingement cases. As they produced significantly different results from the finer meshes, the resolution is likely too low to capture all the relevant physics in the case of droplet impingement. This may explain why the divergence occured, as the resolution was too low. As the resolution of the fine wall film mesh was not significantly higher in the near-wall cells, the resolution of the fine mesh is likely very close to the minimum possible resolution to be used for wall film simulation. For all simulations of wall films, the fine mesh was thus used.

5.2 Impingement Validation

This section describes the results from the simulations of droplets impinging onto a variation of surfaces and how they compare to experimental results from Rioboo et al. (2002) and Šikalo, Wilhelm, Roisman, Jakirlić, and Tropea (2005). As there is only one set of experimental results for each case, there is not way of validating the experimental results. But for the purpose of the simulation validation, the experimental results are considered to be true. It is not described in detail how the spread has been measured in the experiments. Thus, there might be some differences in how the spread is measured between the experiments and the simulations.

5.2.1 Plane Impingement Validation

Spread factor evolution of a water droplets impinging on surfaces is compared to experimental data from Rioboo et al. (2002). The results for the four different cases introduced in Table 4.3 are presented below. Figure 5.2 shows the droplet spread evolution for the first case where the droplet impinges at $We = 52$ onto a hydrophobic wax surface. What can be seen is that as the droplet impacts the surface, an initial spread is induced and continues until a certain point when the droplet instead starts to recede back towards the point of impact. For this case, with a hydrophobic surface, the receding motion is quite energetic and the droplet creates a jet that finally detaches a smaller droplet, as can be seen in Figure 5.2d.

The spread factor evolution of the droplet is shown in Figure 5.8 for the simulations of static and dynamic contact angle along the experiment. There is a slight overprediction of the maximum spread factor for the simulations both using a static and dynamic contact angle. Although the result is overpredicted the spread follow that of the experiments well. The static contact angle gives a slightly higher maximum spread value, but overall give a very similar result to the dynamic contact angle for the first 30 ms.

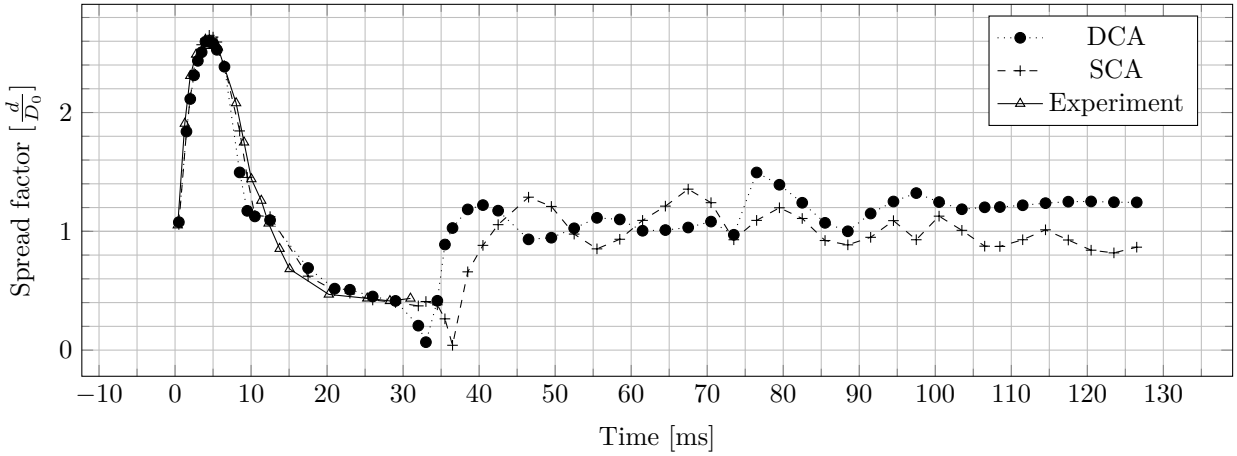

Figure 5.8: *Comparison of spread factor between, simulations of static and dynamic contact angle and experiments for a plane hydrophobic surface, $We = 52$.*

The experimental data is measured until the spread factor is at its lowest, this is when the jet reaches its maximum height and a droplet detaches at the top, which can be seen in Figure 5.2d. However, continuing the simulations past this point gives a difference between the static and dynamic contact angle. The static contact angle seems to get a more energetic jet, so the detached droplet continues to rise, as seen in Figure 5.9, until it finally leaves the domain. Even for an extended domain, the detached droplet still manages to leave the domain. For the dynamic contact angle simulation, the detached droplet continues rising slightly until its upwards motion is overpowered by the gravity and it falls back towards the surface and the detached droplet coalesces with the remaining droplet again at about 70 ms, as can be seen as a fast increase in spread in Figure 5.8. The spread then fluctuates for a few more milliseconds until it stabilises. The static contact angle simulation does not show the coalescing as the detached droplet left the domain and therefore never returns back down. The remaining droplet never reaches a stable condition, but continues to oscillate.

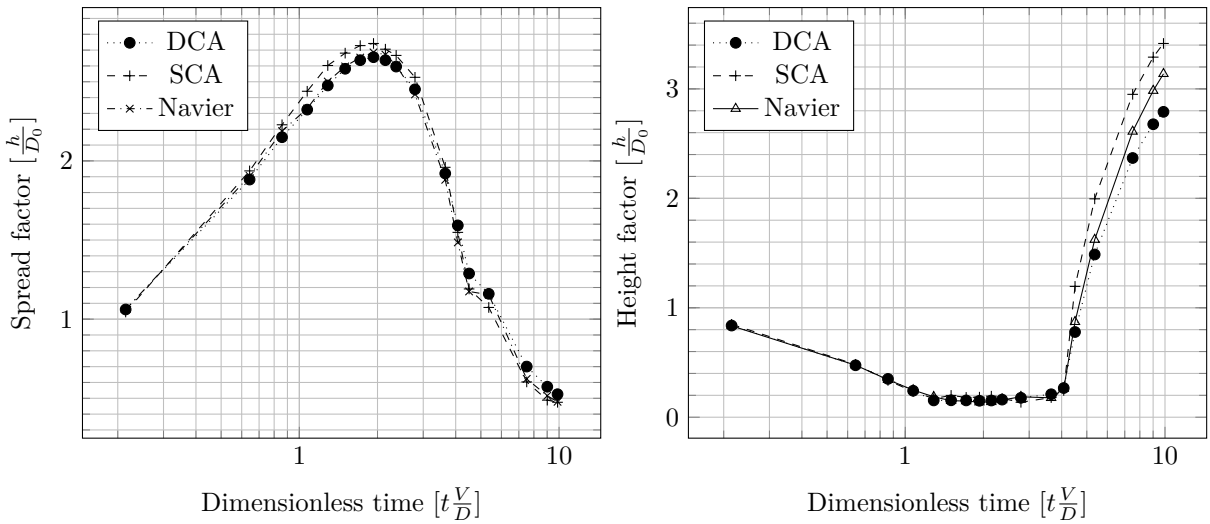

Figure 5.9: *Comparison of height factor between, simulations of static and dynamic contact angle a hydrophobic plane surface, $We = 52$.*

The fact that the static and dynamic contact angle simulations give similar results for the initial spread is not surprising as the impingement is inertia driven and the capillary effects of the surface could be neglected. When the initial spread is done, the inertia will no longer be as dominant and the contact angle model affect the solution more which can be seen as the the two models results start varying.

With a higher Weber number, the energy upon impingement is much higher. For the case of impingement onto a hydrophobic wax surface and $We = 563$, the increased energy results in a splash, as can be seen in Figure 5.10a. The splashing means that there are many small droplets that are moving with high speed from the center of domain. This results in the spread factor being hard to measure as there is no clear diameter as for the previous case. The experiential results presented in Rioboo et al. (2002) does not show this splashing effect, but show more of a slight lamellar spread. Therefore, there is no reason to try to measure the spread of the splash to comparing with the experimental spread as the results are already determined to be non matching with the experimental result.

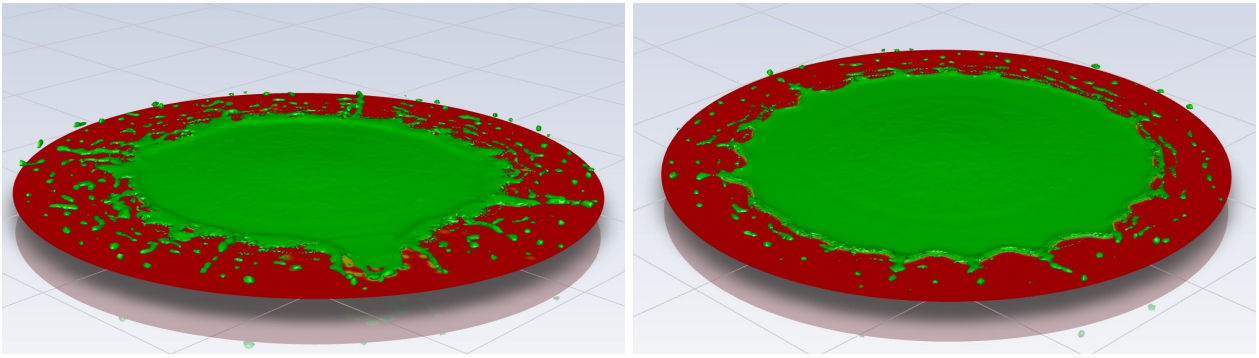

(a) *No-slip boundary condition* **(b)** *Navier-slip boundary condition*

Figure 5.10: *Iso-surface plot of splash on a hydrophobic for* $\alpha = 0.5$ *and* $We = 563$ *at 1.5 ms from impact*

When introducing the Navier-slip the splash becomes less pronounced, as can be seen in Figure 5.10b. These results are tending towards a lamellar spread although still with some splashing. From the experiments, it is not clear if some splashing of small droplets occur, if so the Navier-slip results could be a good match. This would indicate that the properties of the surface affect the initial impingement behaviour as well as the spread along the surface. Further studies on the effect of the mesh and slip dependency has to be done for any conclusions to be drawn about the dynamic contact angle models validity for high Weber number impacts.

For the simulation of droplet impingement onto a hydrophilic surface at a Weber number of 58, the simulated and experimental results does not match, as can be seen in Figure 5.11. The static and dynamic contact angle simulations give nearly identical results, which are highly overpredicted when it come to spread factor. Malgarinos et al. (2014) have done a similar comparison between the experimental data from Rioboo et al. (2002) and a few different dynamic contact angle simulations, and for the specific case of a hydrophilic surface at a Weber number of 58 all simulations resulted in much higher spread than for the experiment as well, although other cases had good agreement. As the glass surface has a contact angle of 10 degrees, which could be defined as superhydrophilic, this could mean that the simulations cannot predict the motion of a drop on an extreme surface. Resolving the curvature for such a low contact angle may result in an unstable solution due to the extreme curvatures of the interface. This is not something that was experienced, which could indicate that the software introduces a stabilising criteria that in this case affects the results.

The result of the simulations for impingement onto a glass surface at a higher Weber number, $We = 563$, are found in Figure 5.12. What can be seen is that the spread of the simulations is delayed compared to the experiment, but the evolution shares general shape and converges towards the same spread. The simulated results are still slightly overpredicting the maximum spread but yields much better results than for the lower impact Weber number. The Navier-slip results however are quite high in comparison to the experimental values. As for the previous hydrophilic case, the contact angle is very low and the simulated results can not be fully trusted.

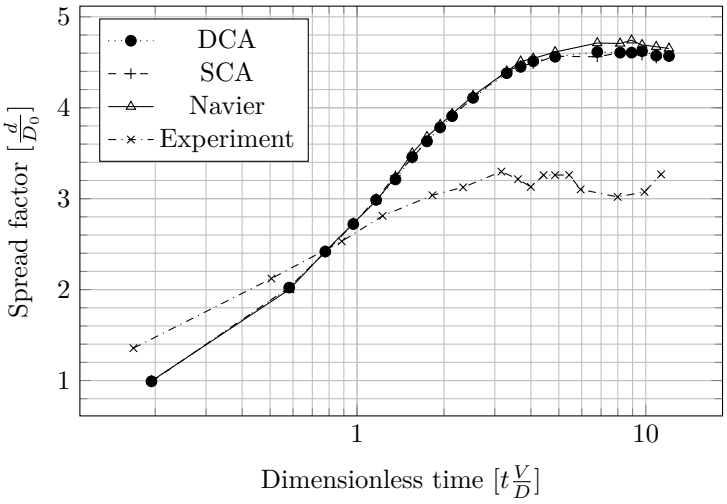

Figure 5.11: *Comparison of spread factor between, simulations of static and dynamic contact angle and experiments for a plane hydrophilic surface,* $We = 58$.

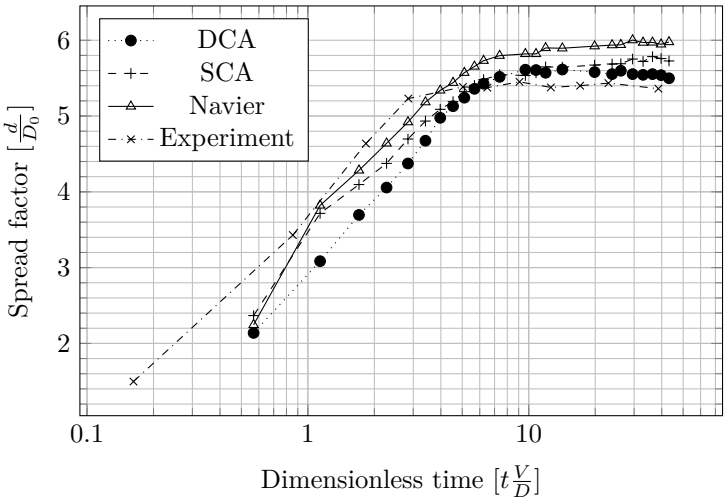

Figure 5.12: *Comparison of spread factor between, simulations of static and dynamic contact angle and experiments for a plane hydrophilic surface,* $We = 563$.

One possible reason for why the high Weber number simulation performs better than the lower one could be due to parasitic currents. For higher Weber numbers, the parasitic current effect on the spread evolution is less as the impingement velocity is higher. For lower impingement velocities, these parasitic currents become more dominant and could cause unrealistic pressure fields that affects the spread.

For all cases the static and dynamic contact angle simulations give similar results, all overpredicting the spread by a varying amount. Introducing the Navier-slip relaxes the stress along the wall, which results in a higher spread factor, which is not the desired results. For the high Weber number impingement onto a hydrophobic surface however the Navier-slip seems to give better results although still splashing. The hydrophilic simulations are hard to consider as the contact angle is so low that the simulations are expected to be unstable. It would be beneficial to have experimental data for impingement onto a surface that is higher than 10° but still hydrophilic. This would give insight to whether the dynamic contact angle can predict the behaviour of spread for hydrophilic surfaces that are not in the superhydrophilic range or if it is struggling for hydrophilic surfaces in general.

5.2.2 Inclined Impingement Validation

Spread factor evolution of a water droplet impinging on 45° and 80° inclined glass and wax surfaces were measured and compared using a variation of set-up conditions in ANSYS Fluent. Simulations were run using static contact angles and a no-slip wall boundary condition, but also the implemented dynamic contact angle model along with both a no-slip and a Navier-slip wall boundary condition. Four different cases are simulated and may be referenced in Table 4.4. The simulated results are compared with experimental data from Šikalo, Tropea, and Ganić (2005), presented as rear and frontal spread. Two different impinging Weber numbers, $We = 50$ and $We = 391$ are compared as well as a variation in hydrophobicity. For all impingement data, the rear and frontal spread factors for the static contact angles, dynamic contact angle model with no-slip and dynamic contact angle with Navier-slip are denoted with front or rear, as well as with SCA, DCA or Nav, respectively. The experimental measurements are denoted with Exp.

Figure 5.13 shows the droplet shape evolution for Case 5, i.e. inclined droplet impingment at $We = 50$ onto a 45° inclined hydrophobic wax surface. As the droplet impacts the surface, there is an initial spread phase which is followed by a retraction of the droplet along its longitudinal axis. As the droplet impinges on the surface, the hydrophobicity of the wax surface causes it to slide down and elongate along the longitudinal axis of the droplet.

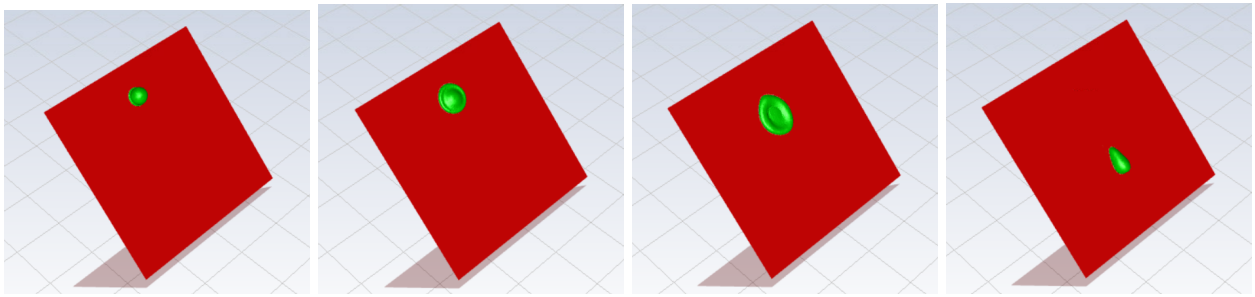

(a) *1.7 ms* **(b)** *3 ms* **(c)** *8 ms* **(d)** *24 ms*

Figure 5.13: *Iso-surface plot of inclined droplet spread evolution for* $\alpha = 0.5$*,* $We = 50$ *and* $\varphi = 45$*.*

The spread factor evolution for this case can be seen in Figure 5.14a at $We = 50$. As can be seen, there is only a slight difference between the simulations as they all predict the expected rebound behaviour. Using the dynamic contact angle model with no-slip, an overprediction can be seen for the frontal spread factor. This can also be seen using both the static contact angles and the dynamic contact angle model with Navier-slip, which also shows a slight overprediction at the later stages of the droplet impingement. For the rear spread factor, all simulations show excellent prediction of the expected behaviour. For inclined droplet impingement at $We = 391$ onto a 45° inclined hydrophobic wax surface, shown in Figure 5.14b, there are larger differences between the simulations. For the frontal spread factor, both the dynamic contact angle model with no-slip and when using static contact angles significantly overpredicts the expected results. The dynamic contact angle model using Navier-slip shows a different development of the spread factor evolution than the experimental results, but provides excellent prediction in the later stages of droplet impingement. For the rear spread factor, the static contact angles fail to predict that the rear of the droplet should slide past the point of impact. Both simulations using the dynamic contact angle model show this sliding behaviour, but it is most correctly predicted by the dynamic contact angle model with no-slip. For the $We = 391$ impingement, all droplets exhibit lamellar structures, where they splash and form small lamella, preferentially in the impact direction, and can be seen in Figure 5.16. These lamella give rise to several smaller droplets, likely due to interfacial instabilities.

For case 6, i.e. inclined droplet impingement onto a 45° inclined hydrophilic glass surface, the droplets fully deposit onto the surface at $We = 50$. The spread factor evolution can be seen in Figure 5.15a. For the frontal spread factor, all simulations show an overprediction, but it is most extreme when using static contact angles. There is a slight improvement in the frontal spread factor when using the Navier-slip boundary condition for the dynamic contact angle model. For the rear spread factor, all simulations overpredict the rear spread factor, as it spreads too far up on the inclined surface. The dynamic contact angle model provides the best prediction, but there is no difference in using a Navier- or no-slip wall boundary condition. For $We = 391$ impingement

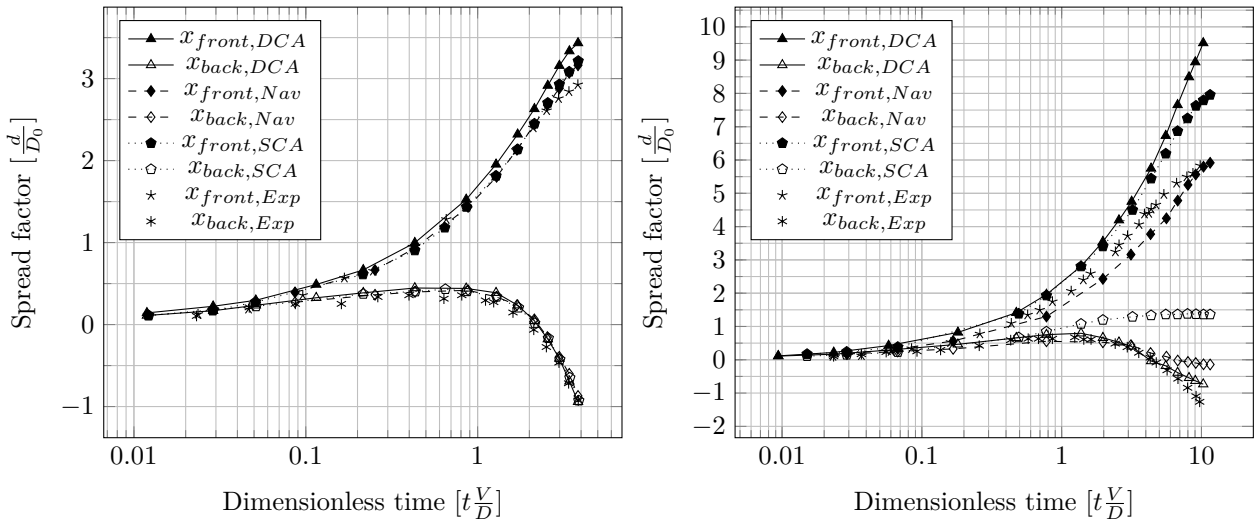

(a) $We = 50$ **(b)** $We = 391$

Figure 5.14: *Comparison of frontal and rear spread factors for experiments and simulations using static contact angles and dynamic contact angles using no-slip and Navier-slip wall boundary conditions. The impingement is shown for a variation of Weber numbers onto a* 45° *inclined wax surface,* $\theta_R = 95°$, $\theta_{eq} = 105°$.

onto a 45° inclined hydrophilic glass surface, shown in Figure 5.15b, all simulations result in a deposition of the droplet upon the surface. Using both the dynamic contact angle model with no-slip and when using static contact angles significantly overpredicts the frontal spread factor. The dynamic contact angle model with Navier-slip slightly overpredicts the experimental results, but by far provides the best results. For the rear spread factor, all models overpredict the spread factor, as it again spreads too far up on the inclined surface. There is a slight improvement when using the dynamic contact angle model with Navier-slip. As previously discussed, this could be caused by the very low contact angle of a glass surface not being properly resolved due to instabilities of the curvature.

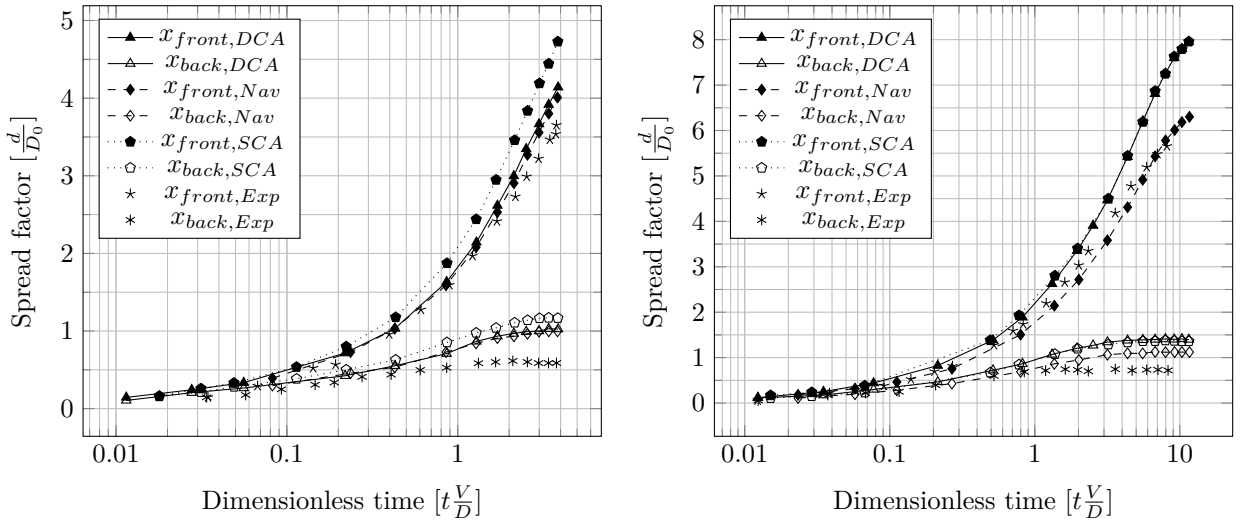

(a) $We = 50$ **(b)** $We = 391$

Figure 5.15: *Comparison of frontal and rear spread factors for experiments and simulations using static contact angles and dynamic contact angles using no-slip and Navier-slip wall boundary conditions. The impingement is shown for a variation of Weber numbers onto a* 45° *inclined glass surface,* $\theta_R = 6°$, $\theta_{eq} = 10°$.

Figure 5.16 shows the later stages of case 5, inclined droplet impingement onto a 45° inclined hydrophobic

surface at $We = 391$. Due to the high energy of the impingement, the droplet forms several smaller lamella during impact. The smallest droplets which are launched away during the impact are neglected, and only the water which is in contact with the surface is taken into account.

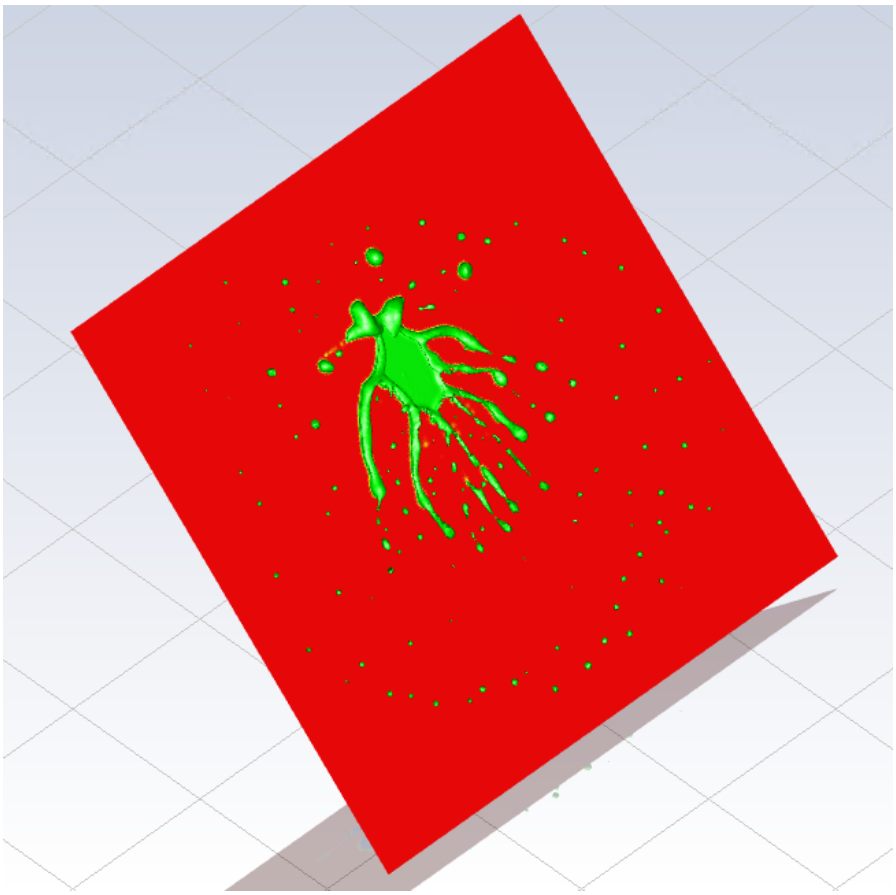

Figure 5.16: *Iso-surface plot of inclined splash for* $\alpha = 0.5$ *and* $We = 391$

The spread factor evolution for case 7, i.e. inclined droplet impingement onto a 80° inclined hydrophobic wax surface can be seen in Figure 5.17a for $We = 50$. For this Weber number, all simulations predicted the expected rebound behaviour. For the frontal spread factor, using static contact angles leads to an overprediction of the expected results. The dynamic contact angle model using no-slip leads to an under-prediction of the expected results. Using the dynamic contact angle model in conjunction with the Navier-slip boundary condition provides the best prediction of the frontal spread factor evolution. For the rear spread factor, the same general spread factor evolution can be seen. An overprediction with static contact angles, an under-prediction with the dynamic contact angle model using no-slip, and the best prediction can be seen using the dynamic contact angle model using Navier-slip. Inclined droplet impingement at $We = 391$ onto a 80° inclined hydrophobic wax surface can be seen in Figure 5.17b. At this Weber number, the static contact angles and the dynamic contact angle model predicted the expected rebound behaviour. For the frontal spread factor, the dynamic contact angle model using no-slip and when using static contact angles show overpredictions of the frontal spread factor, but there is no discernible difference between the two results. Using the dynamic contact angle model with Navier-slip shows a slight overprediction of the experimental results for the frontal spread factor. For the rear spread factor, the same general behaviour may be seen. A slight overprediction using the dynamic contact angle model with no-slip, and when using static contact angles. The dynamic contact angle model with Navier-slip slightly overpredicts the sliding of the droplet, as can be seen in the rear spread factor. However, it shows the best prediction of the experimental results.

Spread factor evolution for case 8, i.e. inclined droplet impingement onto a 80° inclined hydrophilic glass surface may be seen in Figure 5.18a for $We = 50$. At this Weber number, all simulations resulted in a

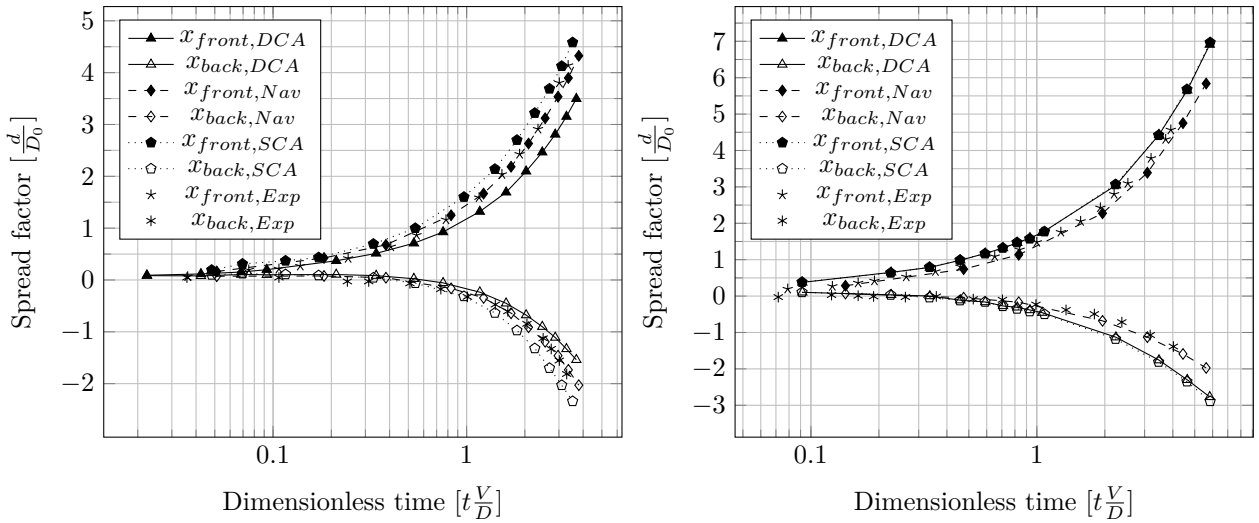

(a) $We = 50$ **(b)** $We = 391$

Figure 5.17: *Comparison of frontal and rear spread factors for experiments and simulations using static contact angles and dynamic contact angles using no-slip and Navier-slip wall boundary conditions. The impingement is shown for a variation of Weber numbers onto a* $80°$ *inclined wax surface,* $\theta_R = 95°$, $\theta_{adv} = 105°$.

deposition upon the surface. For the frontal spread factor, all the simulations show a slight overprediction of the expected results, and there is almost no discernible difference between the simulations. For the rear spread factor, all simulations show an under-prediction in comparison to the experimental results. This is due to the fact that the rear spread factor does not recede over the surface as can be seen in the experiments. For case 8 using $We = 391$, all impinging droplets deposited onto the surface. The frontal spread factor is under-predicted when using static contact angles. There is almost no discernible difference when using Navier- or no-slip boundary conditions for the dynamic contact angle, but they both provide excellent prediction of the experimental results. The rear spread factor is predicted well by all simulations.

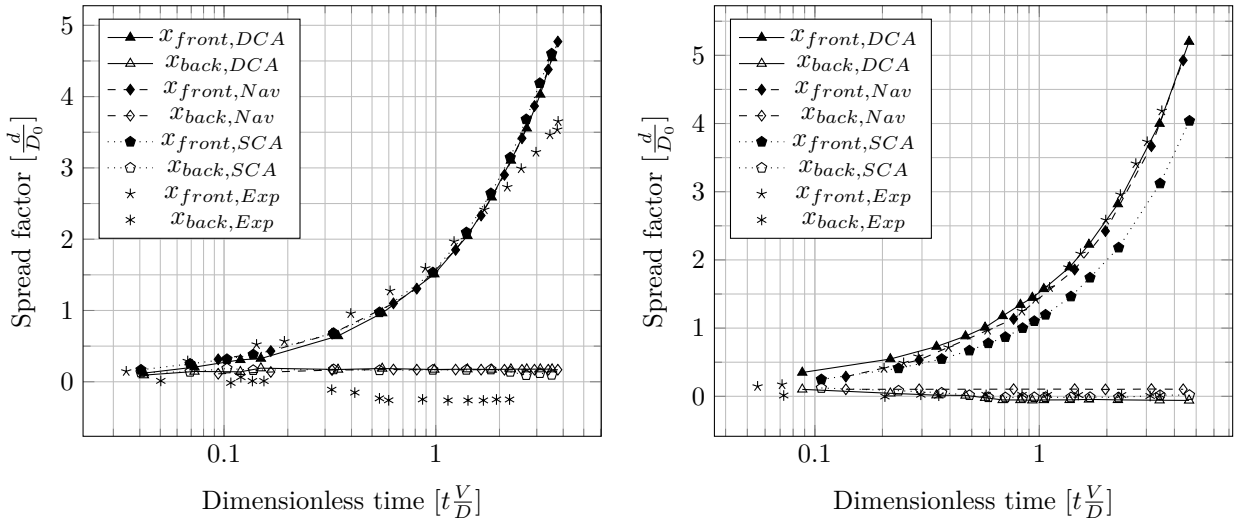

(a) $We = 50$ **(b)** $We = 391$

Figure 5.18: *Comparison of frontal and rear spread factors for experiments and simulations using static contact angles and dynamic contact angles using no-slip and Navier-slip wall boundary conditions. The impingement is shown for a variation of Weber numbers onto a* $80°$ *inclined glass surface,* $\theta_R = 6°$, $\theta_{adv} = 10°$.

The simulated results generally match closely with the experimental results, and the expected physical be-

haviour of droplet rebound, lamellar spread or deposition could be seen for all the simulations. As the general droplet behaviour is correctly predicted using both static contact angles, or using the dynamic contact angle model, with no-slip and Navier-slip, results generally follow the experimental results for all cases. There is however almost always an improvement in using the dynamic contact angle model. When using Navier-slip, this improvement becomes more pronounced, as in almost all cases, the dynamic contact angle model with Navier-slip provides the most accurate prediction of the experimental results.

In general, the relaxation of the no-slip condition relaxes the shear stress singularity which occurs at no-slip boundaries. It should also cause an increase in spreading, as the resistance encountered by the droplet is lower as it is allowed to slip over the dry surface. This was not seen for the inclined droplet impingement cases, as there is no clear correlation between using the Navier-slip, and a reduction in the frontal or rear spread factors. This is different from what could be seen for the plane impingement cases, where the use of Navier-slip resulted in a slightly higher spread factor.

In contrast to the plane droplet impingement case, inclined droplet impingement with Navier-slip was more successfully predicted the rear and frontal spread factors for low Weber number droplet impingement. One reason why this may be the case is the increased significance of the gravitational forces for the inclined droplet impingement, as the gravitational vector is more in line with the spread direction of the droplet. This would yield an increased contribution by the gravitational forces to the contact line velocity in the spread direction. As the significance of the gravitational forces increase, the dynamics of the inclined droplet impingement may become less dominant by other forces which are more prevalent in the plane droplet impingement.

Comparing the inclined droplet impingement for different hydrophobicites, it can clearly be seen that the hydrophobicity of the impingement surface has significant results on the spread factor evolution of the droplet, and in turn, the final wetting of the surface. For the hydrophobic surfaces, impingement of droplets at $We = 50$ resulted in a rebound off of the surface. As the spread factors in a rebound are much lower than in a deposition, splash or lamellar spread, the total wetting occuring on the surface will be much smaller. For droplets impinging a hydrophobic surface at $We = 391$, rebound occured on the 80° inclined surface, but lamellar spread occured on the 45° inclined surface. This indicates that the higher wall-normal velocity of the 45° inclined surface increases the prevalence of lamellar spread impacts. In comparing the lamellar and rebound phenomena, it was clearly seen that the rebound resulted in an increased spreading in the longitudinal direction of the droplet, whereas for the lamellar spread, the width of the spread was far larger. This may also give rise to increased total wetting of the surface. In the case of lamellar spread, several smaller droplets were launched of during the impact. These smaller droplets subsequently deposited onto the surface. Thus, for the droplets exhibiting lamellar spread, several smaller droplets deposit and wet the surface. For the hydrophilic surfaces, all impinging droplets deposited onto the surface. With increasing Weber number, higher spread factors were seen for the 45° impingement case, but not for the 80° case. However, these differences were very small. In general, for a hydrophilic surface, significant wetting will occur as the droplets will impact and form a film.

5.3 Wall Film

Figure 5.19 shows a comparison between using the Dynamic contact angle model with a Navier-slip wall boundary condition, and using static contact angles. As can be seen, as the water is in contact with the hydrophobic wall surface, surface tension causes it to contract into a rivulet. As it reaches the hydrophilic glass surface, the water spreads into a film covering large parts of the surface. There is a slight difference in how the dynamic contact angle model and the static contact angle spreads over the glass surface. Although no conclusions can be drawn from this difference as the spread in not properly measured and validated, there is a difference to be seen. This would indicate that the dynamic contact angle model provides a variance in contact angle on the surface as the liquid moves.

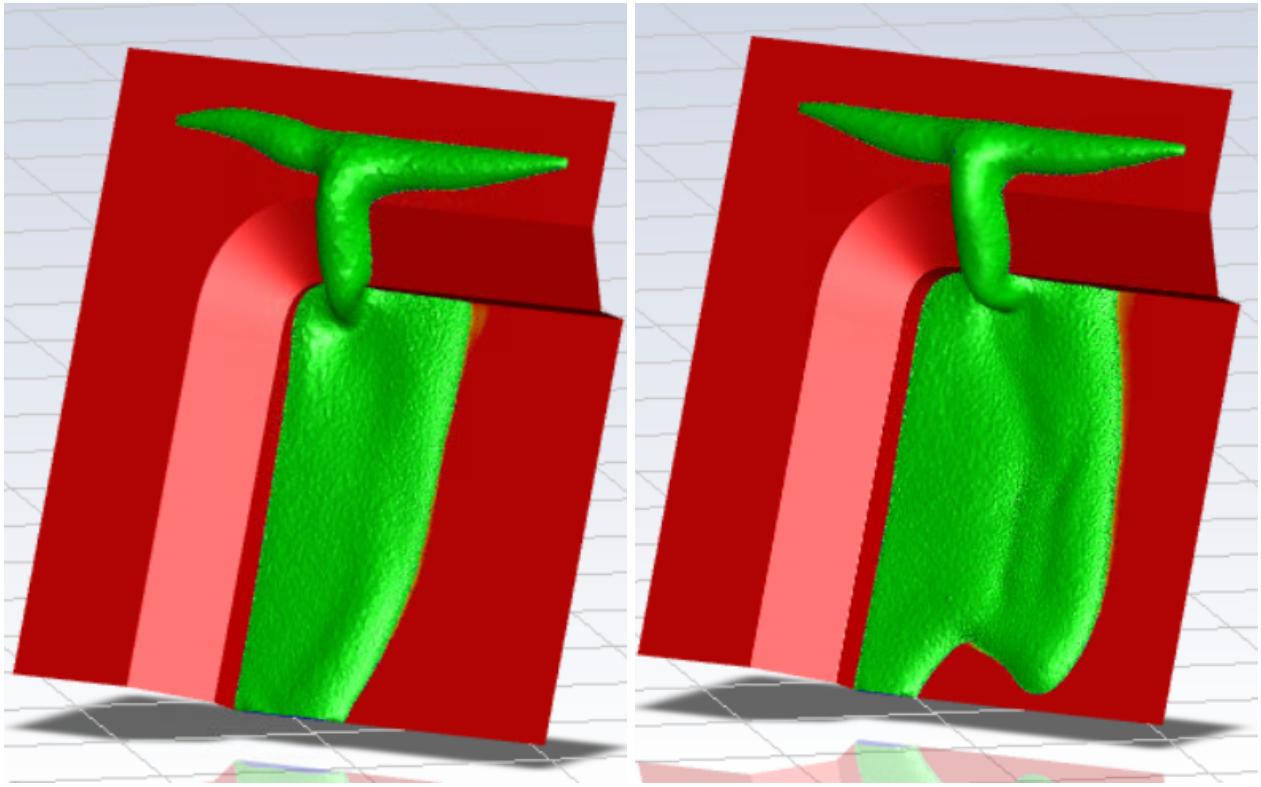

(a) *Dynamic contact angle model.* **(b)** *Static contact angles.*

Figure 5.19: *Iso-surface plot of water film for* $\alpha = 0.5$ *using dynamic contact angle or static contact angle, on a polyhedral mesh with refined near-wall cells.* $\theta_A = 95°$, $\theta_R = 85°$ *for the wall surface, and* $\theta_A = 35°$, $\theta_R = 25°$ *for the glass surface.*

Notable here is that a polyhedral mesh with refined near-wall cells was used although this approach did not give good results for the droplet impingement. As the water film simulations can not be validated against any experiment, there is no way of knowing if the simulated results are realistic. In general, the results of the wall film simulation should be viewed as a proof of concept, as they are not representative of the film behaviour which is to be expected from rain, nor are there any experimental results available for comparison and validation. The results however do prove that the dynamic contact angle model is capable of handling complex geometry and surfaces with different hydrophobicity. This is of paramount importance if the model is to be used to model water film behaviour on real geometry.

6 Conclusion

Film contamination on dry surfaces may occur as a product of rain, which was evaluated in the form of singular droplets impacting dry surfaces with different inclination. As droplets impinge on the surface, the physics of the impact is highly driven by inertial forces. For a fully or partially wet surface, this may not be the case, as viscous forces may be significant.

Simulations using the user defined function of a dynamic contact angle model generally predicted the impingement physics well. However, for hydrophilic surfaces the results did not match well with experimental data. This is likely not due to the dynamic contact angle model but the instability of resolving the curvature for low contact angles. Additionally, for high Weber number impingement, splash phenomena not seen in experiments occurs. Visually, using a Navier-slip wall boundary condition appears to reduce this splash phenomenon. For inclined impingement, simulations generally followed the experimental results more closely, which may be due to the increased significance of the gravitational forces in inclined impingement.

Droplet impingement proved to be very dependent on the choice of mesh. Mesh convergence studies were conducted for polyhedral meshes with different types near-wall refinement. Conclusively, the mesh study showed that high resolution was needed near the walls, specifically a first cell height of 4 ± 1.5 micrometers depending on the case. In the case of plane and inclined droplet impingement the refinement approach providing the best results was done by prism layers.

The water film was not representative of the surface wetting which might occur from rain film contamination. However, it was shown as a proof of concept, in order to evaluate how the implemented model handled complex geometries, as well as geometries with different hydrophobicities.

6.1 Future Work

For the future it would be beneficial to continue investigating the strategy for meshing the boundary layer and what differs between the prism layer and refined near-wall cell approach. This could include a study of what instabilities are introduced in the boundary layers and how is the symmetry broken in the prism layers. It would also be beneficial to look further into the splashing for high Weber numbers and how Navier-slip limits the splash. Additional experiments could also be done to validate the experimental data of Rioboo et al. (2002).

Another work for the future would be to first, continue the water film modelling, and to validate it to a experimental results in order to see if the model is also viable for water films. This would be important as the dynamics of the droplet impingement are highly dominated by inertial forces, and as a water film would most likely exhibit a much lower velocity, the prevalence of other forces, such as viscous forces may increase.

Furthermore, as the use of the VOF model places incredible demands on the temporal and spatial resolution of the domain, means to reduce this should be investigated. One way of doing this would be to use a coupled DPM-VOF simulation, where the droplet is tracked as a lagrangian particle. This would enable the simulation of multiple droplets impingement. As the droplets impinge on the surface, they would form a lagrangian film, and when the volume fraction of water in the near-wall cells exceeds a specific value, a VOF film may be formed. For this film, the implemented dynamic contact angle model may be used in order to predict the wetting of the surface. As of writing this report, there is no such methodology implemented in ANSYS Fluent. Another alternative would be to induce the rain using DPM and transfer the droplets to VOF just above the surface, so that the impingement physics could be considered. It would also be interesting to compare these results to those where the DPM to VOF transfer goes through the lagrangian film model to analyse if the impingement affects the film build up.

References

Afkhami, S., Zaleski, S., & Bussmann, M. (2009). A mesh-dependent model for applying dynamic contact angles to vof simulations. *Journal of computational physics*, *228*(15), 5370–5389.

Ansys fluent customization manual [Computer software manual]. (2020).

Ansys theory guide [Computer software manual]. (2020).

Ansys user guide [Computer software manual]. (2020).

Bilanin, A. J. (1987). Scaling laws for testing airfoils under heavy rainfall. *Journal of Aircraft*, *24*(1), 31–37.

Brackbill, J. U., Kothe, D. B., & Zemach, C. (1992). A continuum method for modeling surface tension. *Journal of computational physics*, *100*(2), 335–354.

Cerwall, P., Jonsson, P., Carson, S., Blennerud, G., Kyohun Shim, J., Arendse, B., ... Öhman, K. (2019). *Ericsson mobility report november 2019.*

Cox, R. (1986). The dynamics of the spreading of liquids on a solid surface. part 1. viscous flow. *Journal of fluid mechanics*, *168*, 169–194.

de Gennes, P., Brochard-Wyart, F., & Quere, D. (2003). *Capillarity and wetting phenomena: Drops, bubbles, pearls, waves*. Springer New York.

Dupont, J.-B., & Legendre, D. (2010). Numerical simulation of static and sliding drop with contact angle hysteresis. *Journal of Computational Physics*, *229*(7), 2453–2478.

Ersoy, N. E., & Eslamian, M. (2020). Phenomenological study and comparison of droplet impact dynamics on a dry surface, thin liquid film, liquid film and shallow pool. *Experimental Thermal and Fluid Science*, *112*, 109977.

Fenn, A. (1997). Measurements of wet radome transmission loss and depolarization effects in simulated rain at 20 ghz. In *Tenth international conference on antennas and propagation (conf. publ. no. 436)* (Vol. 1, pp. 474–477).

Gariboldi, C., & Takahashi, T. (2019). Asymptotic analysis of an optimal control problem for a viscous incompressible fluid with navier slip boundary conditions. *arXiv preprint arXiv:1910.11699*.

Göhl, J., Mark, A., Sasic, S., & Edelvik, F. (2018). An immersed boundary based dynamic contact angle framework for handling complex surfaces of mixed wettabilities. *International Journal of Multiphase Flow*, *109*, 164–177.

Grémont, B. C., & Filip, M. (2004). Spatio-temporal rain attenuation model for application to fade mitigation techniques. *IEEE transactions on antennas and propagation*, *52*(5), 1245–1256.

Hirt, C. W., & Nichols, B. D. (1981). Volume of fluid (vof) method for the dynamics of free boundaries. *Journal of computational physics*, *39*(1), 201–225.

Hoffman, R. L. (1975). A study of the advancing interface. i. interface shape in liquid—gas systems. *Journal of colloid and interface science*, *50*(2), 228–241.

Jebson, S. (2007). Fact sheet number 3: Water in the atmosphere.

Kistler, S. F. (1993). Hydrodynamics of wetting. *Wettability*, *6*, 311–430.

Legendre, D., & Maglio, M. (2015). Comparison between numerical models for the simulation of moving contact lines. *Computers & Fluids*, *113*, 2–13.

Malgarinos, I., Nikolopoulos, N., Marengo, M., Antonini, C., & Gavaises, M. (2014). Vof simulations of the contact angle dynamics during the drop spreading: Standard models and a new wetting force model. *Advances in colloid and interface science*, *212*, 1–20.

Mathieu, B. (2003). *Etudes physique, expérimentale et numérique des mécanismes de base intervenant dans les écoulements diphasiques* (Unpublished doctoral dissertation). Aix-Marseille 1.

Meredith, K., Heather, A., De Vries, J., & Xin, Y. (2011). A numerical model for partially-wetted flow of thin liquid films. *Computational Methods in Multiphase Flow VI*, *70*, 239.

Moreira, A., Moita, A., & Panao, M. (2010). Advances and challenges in explaining fuel spray impingement: How much of single droplet impact research is useful? *Progress in energy and combustion science*, *36*(5), 554–580.

Moroder, C., Siart, U., Chwala, C., & Kunstmann, H. (2017). Fundamental study of wet antenna attenuation. In *Proc. 15th int. conf. environ. sci. technol.* (pp. 1–4).

Nichita, B. A., Zun, I., & Thome, J. R. (2010). A vof method coupled with a dynamic contact angle model for simulation of two-phase flows with partial wetting. In *7th international conference on multiphase flow, icmf 2010, tampa, fl, may 30–june 4, 2010.*

Nouhou Bako, A., Darboux, F., James, F., Josserand, C., & Lucas, C. (2016). Pressure and shear stress caused by raindrop impact at the soil surface: Scaling laws depending on the water depth. *Earth Surface Processes and Landforms*, *41*(9), 1199–1210.

Rapp, B. (2016). *Microfluidics: Modeling, mechanics and mathematics.*

Rein, M. (1993). Phenomena of liquid drop impact on solid and liquid surfaces. *Fluid Dynamics Research*, *12*(2), 61.

Renardy, M., Renardy, Y., & Li, J. (2001). Numerical simulation of moving contact line problems using a volume-of-fluid method. *Journal of Computational Physics*, *171*(1), 243–263.

Rioboo, R., Marengo, M., & Tropea, C. (2002). Time evolution of liquid drop impact onto solid, dry surfaces. *Experiments in fluids*, *33*(1), 112–124.

Salazar-Cerreño, J. L., Chandrasekar, V., Trabal, J. M., Siquera, P., Medina, R., Knapp, E., & McLaughlin, D. J. (2014). A drop size distribution (dsd)-based model for evaluating the performance of wet radomes for dual-polarized radars. *Journal of Atmospheric and Oceanic Technology*, *31*(11), 2409–2430.

Schiaffino, S., & Sonin, A. A. (1997). Molten droplet deposition and solidification at low weber numbers. *Physics of fluids*, *9*(11), 3172–3187.

Serio, M. A., Carollo, F. G., & Ferro, V. (2019). Raindrop size distribution and terminal velocity for rainfall erosivity studies. a review. *Journal of Hydrology*.

Shikhmurzaev, Y. D. (2007). *Capillary flows with forming interfaces.* Chapman and Hall/CRC.

Šikalo, Š., Tropea, C., & Ganić, E. (2005). Impact of droplets onto inclined surfaces. *Journal of colloid and interface science*, *286*(2), 661–669.

Šikalo, Š., Wilhelm, H.-D., Roisman, I., Jakirlić, S., & Tropea, C. (2005). Dynamic contact angle of spreading droplets: Experiments and simulations. *Physics of Fluids*, *17*(6), 062103.

Tanner, L. (1979). The spreading of silicone oil drops on horizontal surfaces. *Journal of Physics D: Applied Physics*, *12*(9), 1473.

Weigand, R. (1973). Performance of a water-repellent radome coating in an airport surveillance radar. *Proceedings of the IEEE*, *61*(8), 1167–1168.

Wu, Z. (2018). Drop "impact" on an airfoil surface. *Advances in colloid and interface science*, *256*, 23–47.

Yadigaroglu, G., & Hewitt, G. F. (2017). *Introduction to multiphase flow: Basic concepts, applications and modelling* (1st ed.). Springer Publishing Company, Incorporated.

Yamamoto, K., Motosuke, M., & Ogata, S. (2018). Initiation of the worthington jet on the droplet impact. *Applied Physics Letters*, *112*(9), 093701.

Young, T. (1805). Iii. an essay on the cohesion of fluids. *Philosophical transactions of the royal society of London*(95), 65–87.

Zhou, W., Loney, D. A., Fedorov, A. G., Degertekin, F. L., & Rosen, D. W. (2012). Droplet impingement dynamics in ink-jet deposition: A novel measure of droplet shape characterization for the optimization of droplet deposition process is proposed in this paper. *Virtual and Physical Prototyping*, *7*(1), 49–64.

A User Defined Function

This is an example of the created user defined function, where a hydrophobic surface with a contact angle of 100 degrees and a Navier slip is defined. The contact angle can easily by changed and can be varied for different surfaces using the surface IDs from ANSYS Fluent. The Navier slip can be changed to a regular no-slip by changing u_cell to be just the velocity of the cell under the Navier slip section.

```
#include "udf.h"

/*********************************************/
/* Dynamic Contact UDF                       */
/* Last Updated: 2020/06/04                  */
/* By Love Eriksson and Patricia Vanky       */
/* Modified 2020/02/27 Adam Anderson ANSYS UK */
/*********************************************/


/*********************/
/*  Model Parameters */
/*********************/

typedef enum{
  HYDROPHILIC,
  HYDROPHOBIC,
  N_HYDRO_TYPES
}HydroType;

/* Hydrophilic and hydrophobic parameters are stored in arrays. */
static double theta_ed_ar[N_HYDRO_TYPES] = {100.0, 100.0};   /* Static contact
   ↪ angle[degree]*/
static double mu_ar[N_HYDRO_TYPES] = {0.001003, 0.001003}; /* Viscosity
   ↪ coefficient[kg/m-s] */
static double sigma_ar[N_HYDRO_TYPES] = {0.0728, 0.0728};  /* Surface tension
   ↪ coefficient [N/m] */
static double theta_a_ar[N_HYDRO_TYPES] = {105.0, 105.0};    /* Maximum advance
   ↪  angle [degree] */
static double theta_r_ar[N_HYDRO_TYPES] = {95.0, 95.0};    /* Minimum receding
   ↪ angle [degree] */

HydroType get_hydro_type(Thread *ft)
{
  /* Helper function to get thread hydro type. */
  /* If surfaces with different hydrophobicites are to be used, "
     ↪ hydrophilic_thread[]" must point to appropriate boundary id.*/
  int i;
  int n_hydrophilic = 1;
  int hydrophilic_threads[] = {23};
  int thread_id;

  thread_id = THREAD_ID(ft);

  for (i=0;i<n_hydrophilic;i++)
    if (thread_id == hydrophilic_threads[i])
      return HYDROPHILIC;

  return HYDROPHOBIC;
```

```
}

/* Enumerate UDM numbers */
enum{
  VOF_G_X,
  VOF_G_Y,
  VOF_G_Z,
  VTFS,
  CONTACT_ANGLE,
  REL_VEL_U,
  REL_VEL_V,
  REL_VEL_W,
  C_ucell,
  C_lambda,
  C_nw,
  C_tw,
  CONTACT_N_REQ_UDM
};

#define C_VOF_G_X(C,T)C_UDMI(C,T,VOF_G_X)
#define C_VOF_G_Y(C,T)C_UDMI(C,T,VOF_G_Y)
#define C_VOF_G_Z(C,T)C_UDMI(C,T,VOF_G_Z)
#define C_VTFS(C,T)C_UDMI(C,T,VTFS)
#define C_CONTACT_ANGLE(C,T)C_UDMI(C,T,CONTACT_ANGLE)
#define C_REL_VEL_U(C,T)C_UDMI(C,T,REL_VEL_U)
#define C_REL_VEL_V(C,T)C_UDMI(C,T,REL_VEL_V)
#define C_REL_VEL_W(C,T)C_UDMI(C,T,REL_VEL_W)
#define C_ucell(C,T)C_UDMI(C,T,C_ucell)
#define C_lambda(C,T)C_UDMI(C,T,C_lambda)
#define C_tw(C,T)C_UDMI(C,T,C_tw)
#define C_nw(C,T)C_UDMI(C,T,C_nw)

DEFINE_ADJUST(dynamic_contact, domain)
{
  Thread *ct, *pct, *t0;
  Thread *ft;
  cell_t c, c0;
  face_t f;

  double theta_n;
  real Vtfs, temp[ND_ND], vel_re[ND_ND], vof_n[ND_ND], vec_nw[ND_ND], vec_tw[
    ↪ ND_ND], vec_snw[ND_ND];
  real vec_ntw[ND_ND], vec_stw[ND_ND], A[ND_ND], Amag, Smag, u_cell[ND_ND],
    ↪ veltan[ND_ND];
  double f_Hoff_inverse, x_hoff, Ca, gapp, xapp, lambda, theta_ed, mu, sigma,
    ↪ theta_a, theta_r;

  int phase_domain_index = 1;
  Domain *pDomain = DOMAIN_SUB_DOMAIN(domain, phase_domain_index);

  HydroType hydro_type;



  if(first_iteration)
    {
```

```
/* Check UDMs have been set up */

if(N_UDM < CONTACT_N_REQ_UDM)
  {
    Message0("\n WARNING: Require at least %d UDMs to be set up for
        ↪ dynamic contact angle model.\n", CONTACT_N_REQ_UDM);
    return;
  }

/* Calculate VOF gradient */

Alloc_Storage_Vars(pDomain,SV_VOF_RG,SV_VOF_G,SV_NULL); /* Primary
    ↪ storage of variables being calculated */
Scalar_Reconstruction(pDomain, SV_VOF,-1,SV_VOF_RG,NULL);
Scalar_Derivatives(pDomain,SV_VOF,-1,SV_VOF_G,SV_VOF_RG,
    ↪ Vof_Deriv_Accumulate);


/* Store VOF gradient in user memory */

thread_loop_c(ct,domain) /* Simpler thread loop */
  if (FLUID_THREAD_P(ct))
    {
      pct = THREAD_SUB_THREAD(ct,phase_domain_index); /* Use this instead
          ↪  of pt[] */

      begin_c_loop (c,ct)
        {
          ND_V(C_VOF_G_X(c,ct),C_VOF_G_Y(c,ct),C_VOF_G_Z(c,ct),=,C_VOF_G(
              ↪ c,pct)); /* Set 3 components to a vector */
        }
      end_c_loop (c,ct)
    }

/* Free memory used for VOF gradient */
Free_Storage_Vars(pDomain,SV_VOF_RG,SV_VOF_G,SV_NULL);


/* Calculate wall contact angle and save to user memory */

thread_loop_f(ft,domain)
  {
    if (THREAD_TYPE(ft) == THREAD_F_WALL) /*Mixture Thread and Wall*/
      {
        t0 = THREAD_T0(ft);

        if(FLUID_THREAD_P(t0))     /* Fluid Zone */
          {
            HydroType hydro_type;

            /* Set contact angle parameters according to the type of wall
                ↪  surface */

            hydro_type = get_hydro_type(ft);

            theta_ed = theta_ed_ar[hydro_type];
```

```
mu = mu_ar[hydro_type];
sigma = sigma_ar[hydro_type];
theta_a = theta_a_ar[hydro_type];
theta_r = theta_r_ar[hydro_type];

begin_f_loop(f,ft)
  {
    c0 = F_C0(f,ft);

    /* Get flow velocity relative to face */
    NV_DD(vel_re,=,C_U(c0,t0),C_V(c0,t0),C_W(c0,t0),-,F_U(f,
        ↪ ft),F_V(f,ft),F_W(f,ft));
    ND_V(C_REL_VEL_U(c0,t0),C_REL_VEL_V(c0,t0),C_REL_VEL_W(c0
        ↪ ,t0),=,vel_re);

     F_AREA(A,f,ft); /* Area vector */
    Amag = NV_MAG(A);
    NV_S(A,/=,Amag); /* A now holds outward face normal */

     /* Navier slip*/
     lambda=(C_VOLUME(c0,t0)/Amag)/2;
     NV_D(u_cell,=,lambda*C_DUDX(c0,t0),lambda*C_DVDY(c0,
         ↪ t0),lambda*C_DWDZ(c0,t0));

     C_lambda(c0,t0)=lambda;
     C_ucell(c0,t0)=NV_MAG(u_cell);

    NV_D(vof_n,=,C_VOF_G_X(c0,t0),C_VOF_G_Y(c0,t0),C_VOF_G_Z(
        ↪ c0,t0));

    /* vof along wall*/

     NV_VS(vec_nw, =, A, *, NV_DOT(vel_re, A)); /* normal
         ↪ relative velocity vector */
     NV_VV(vec_tw, =, vel_re, -, vec_nw);  /* Tangent
         ↪ velocity direction vector */

     C_nw(c0,t0)=NV_MAG(vec_nw);
     C_tw(c0,t0)=NV_MAG(vec_tw);

    NV_VS(vec_snw, =, A, *, NV_DOT(vof_n, A)); /* Vof
        ↪ gradient normal to wall*/
    NV_VV(vec_stw, =, vof_n, -, vec_snw);      /* Vof gradient
        ↪  vector tangential to wall */

     /*Contact line direction*/
    NV_CROSS(temp,u_cell,vec_nw);
    NV_CROSS(veltan,vec_nw,temp);
    /*****************/
    /*Receding: Calculate dynamic contact angle*/
    if(NV_DOT(veltan,vof_n)>0.0)
      {
              Ca = mu * NV_MAG(veltan)/sigma;

                                        /*DRCA model*/
```

```
                                theta_n = DEGREES(cbrt(CUB(RADIANS(theta_r))
                                    ↪ -72.0*Ca));

                                C_CONTACT_ANGLE(c0,t0) = theta_n;/* deg */
                            }
                          else
                            {
                              /*********************/
                              /* Advancing: Calculate dynamic contact angle*/
                                    Ca = mu * NV_MAG(veltan)/sigma;

                                                    /*Kistler's model*/


                                    f_Hoff_inverse = CUB(RADIANS(theta_ed))/72.0 ;
                                    x_hoff = Ca +  f_Hoff_inverse;
                                    theta_n = DEGREES(acos(1.0 - 2.0*tanh(5.16*pow
                                        ↪ ((x_hoff/(1.0 + 1.31*pow(x_hoff,0.99)))
                                        ↪ ,0.706))));

                                    C_CONTACT_ANGLE(c0,t0) = theta_n; /* [degs] */
                            }

                            C_VTFS(c0,t0)=NV_DOT(veltan,vof_n);
                        }
                    end_f_loop(f,t_m)
                }
            }
        }
    }
}

DEFINE_PROFILE(contact_angle,t,i)
{
  face_t f;
  cell_t c0;
  Thread *t0;

  begin_f_loop(f,t)
    {
        c0 = F_C0(f,t);
                t0 = F_C0_THREAD(f, t);

        F_PROFILE(f,t,i) = RADIANS(C_CONTACT_ANGLE(c0,t0)); /* Angle within the
            ↪ liquid in radians */
    }
  end_f_loop(f,t)
}

DEFINE_EXECUTE_AFTER_CASE(set_name, libname)
{
  Message0("Setting UDM names... ");

  Set_User_Memory_Name(VOF_G_X,"VOF Gradient-x");
  Set_User_Memory_Name(VOF_G_Y,"VOF Gradient-y");
  Set_User_Memory_Name(VOF_G_Z,"VOF Gradient-z");
```

```
  Set_User_Memory_Name(VTFS,"Vtfs");
  Set_User_Memory_Name(CONTACT_ANGLE,"Contact Angle [deg]");
  Set_User_Memory_Name(REL_VEL_U,"relative velocity-x");
  Set_User_Memory_Name(REL_VEL_V,"relative velocity-y");
  Set_User_Memory_Name(REL_VEL_W,"relative velocity-z");
  Set_User_Memory_Name(C_ucell,"Magnitude of cell velocity");
  Set_User_Memory_Name(C_lambda,"lambda");
  Set_User_Memory_Name(C_nw,"Magnitude of normal vector");
  Set_User_Memory_Name(C_tw,"Magnitude of tangential vector");
  Message0("Done.\n");
}

DEFINE_ON_DEMAND(check_settings)
{
  Message0( "\n" );
  Message0( "Model parameter values:\n" );
  Message0( "\n" );
  Message0( "  Hydrophilic:\n" );
  Message0( "    theta_ed= %e\n", theta_ed_ar[HYDROPHILIC]);
  Message0( "    mu      = %e\n", mu_ar[HYDROPHILIC]);
  Message0( "    sigma   = %e\n", sigma_ar[HYDROPHILIC]);
  Message0( "    theta_a = %e\n", theta_a_ar[HYDROPHILIC]);
  Message0( "    theta_r = %e\n", theta_r_ar[HYDROPHILIC]);
  Message0( "\n" );
  Message0( "  Hydrophobic:\n" );
  Message0( "    theta_ed= %e\n", theta_ed_ar[HYDROPHOBIC]);
  Message0( "    mu      = %e\n", mu_ar[HYDROPHOBIC]);
  Message0( "    sigma   = %e\n", sigma_ar[HYDROPHOBIC]);
  Message0( "    theta_a = %e\n", theta_a_ar[HYDROPHOBIC]);
  Message0( "    theta_r = %e\n", theta_r_ar[HYDROPHOBIC]);
  Message0( "\n" );
}
```